

CTLSS—An Advanced Electromagnetic Simulation Tool for Designing High-Power Microwave Sources

Simon J. Cooke, *Member, IEEE*, Alfred A. Mondelli, Baruch Levush, *Senior Member, IEEE*, Thomas M. Antonsen, Jr., *Member, IEEE*, David P. Chernin, Thomas H. McClure, David R. Whaley, *Member, IEEE*, and Mark Basten

Abstract—Simulation-based-design (SBD) techniques to achieve “first-pass design success” depend on the development of fast, accurate, realistic models that can handle material properties, geometry, and appropriate boundary conditions. This paper describes a new three-dimensional (3-D) electromagnetic and large-signal simulation tool, Cold-Test and Large-Signal Simulator (CTLSS), which has been developed as part of an SBD tool suite for vacuum electron devices.

Computational electromagnetic codes are essential for applying the SBD methodology to the design of vacuum electron devices and components. CTLSS offers the unique advantage that its computational electromagnetics model is linked intimately with a large-signal simulation tool for computing the electron-wave interaction in the radiating structure. Currently, this link has been implemented for helix traveling-wave tubes (TWT’s) only, using the CHRISTINE code as the large-signal model, but a new, general, large-signal model is under development and is described in this paper.

The electromagnetic simulation engine in CTLSS has been designed and implemented as a volumetric frequency-domain model that can handle both resonant eigenvalue problems, using the Jacobi–Davidson algorithm, and nonresonant driven-frequency problems, using the quasi-minimal residual (QMR) technique to invert the non-Hermitian matrices that often occur in real problems.

The features and advantages of this code relative to other models and results from the code for several classes of microwave devices are presented.

Index Terms—CHRISTINE, computational electromagnetics, CTLSS, high power microwaves, large signal models, modeling and simulation, simulation-based design, vacuum electron devices.

I. INTRODUCTION

A. Simulation Codes for HPM

HIGH-POWER microwave (HPM) research has focused on the development of microwave sources, output windows, and advanced cathodes. An overall goal of HPM research is

to increase device efficiencies and to reduce their weight and volume. Prospective HPM sources include vircators, klystrons, relativistic magnetrons, high-efficiency backward-wave oscillators, and fast-wave gyrodevices. Research continues on new sources, based on plasma-filled devices, ultrawideband technology, and transit-time oscillators. In addition, there are on-going research efforts on advanced cathodes, ferroelectric cathodes, microwave vacuum and window breakdown, and multipactor phenomena to increase the RF vacuum strength of cavities and windows to produce higher energy density and longer pulse devices.

The simulation and virtual prototyping of HPM devices [1] traditionally has fallen into three areas:

- 1) *Pulsed power sources*. These devices create the high-power electrical pulses needed to drive HPM sources. They may be based on very rapid magnetic flux compression by explosively driven liners, for example, and are often modeled with magnetohydrodynamics (MHD) simulation codes.
- 2) *HPM sources*. Particle-in-cell (PIC) simulation codes have been used in the HPM research community to model the interaction of a high-power electron beam with the cavity structure and applied fields in the source.
- 3) *Antennas*. Computational electromagnetics software has been used to model the antenna structure with particular emphasis on mode control to avoid “hot spots,” which lead to RF breakdown and plasma formation.

The development of general electromagnetic and large-signal models, like the Cold-Test and Large-Signal Simulator (CTLSS), will offer the potential to greatly accelerate the development of HPM devices by allowing integrated design calculations of the HPM source, the output coupler, and the antenna, with fast-running large-signal analyzes of the interaction region. The current use of time-consuming PIC models is required because faster parametric models and large-signal models based on averaging over the highest frequencies in the particle motion have not been implemented for novel or exotic HPM sources.

Other electromagnetic eigenvalue codes, such as ARGUS [2] and MAFIA [3], that are used in the vacuum electron device community are based on the Tückmantel algorithm [4], which was formulated for Hermitian systems. Although these codes have been extended to treat lossy materials, they do not converge for loss tangents greater than about 10%. The CTLSS code, described below, has been specifically formulated to handle complex material properties.

Manuscript received October 15, 1999; revised March 13, 2000. This work was supported by the Office of Naval Research under Contract N00014-97-C-2035.

S. J. Cooke, A. A. Mondelli, D. P. Chernin, and T. H. McClure are with the Advanced Technology Group, SAIC, McLean, VA 22102 USA (e-mail: mondellia@saic.com).

B. Levush is with the Vacuum Electronics Branch, Naval Research Laboratory, Washington, DC USA.

T. M. Antonsen, Jr. is with the Institute for Plasma Research, University of Maryland, College Park, MD 20742 USA.

D. R. Whaley and M. Basten are with the Northrop Grumman Corporation, ESSS-DSD, Rolling Meadows, IL USA.

Publisher Item Identifier S 0093-3813(00)05713-1.

B. CTLSS Code Overview

CTLSS has been designed as a state-of-the-art three-dimensional (3-D) simulation model for the electromagnetic and large-signal behavior of vacuum electron devices. It builds on years of development of electromagnetic and large-signal simulation codes, and it has been designed to remedy many shortcomings in existing codes when treating realistic problems involving lossy materials and complex geometry.

The CTLSS model offers many useful features as follows.

- 1) *Meshing.* CTLSS currently uses a 3-D structured, single-block mesh, and it supports orthogonal coordinate systems in both Cartesian and cylindrical geometry. The mesh includes special models to impose sharp-corner corrections on material boundaries. New development in progress will incorporate multiblock, nonorthogonal structured mesh for conformal representation of 3-D structures.
- 2) *Materials.* CTLSS supports inhomogeneous material parameters, with structures mapped to mesh cells. Anisotropic materials with diagonal tensor properties are permitted, and the formulation extends to full tensor material properties. Absorbing materials are included using complex-valued material parameters to represent losses. The CTLSS eigenvalue algorithm successfully operates, even with very large loss tangents ($\tan \delta \approx 100\%$ has been used successfully.) New algorithms for advanced material properties are under development to handle nonlinear and dispersive materials.
- 3) *Boundary conditions.* Block boundary conditions, including perfect electric conductor, perfect magnetic conductor, symmetry wall, periodic, and Floquet periodic with specified phase advance are supported on all three axes. New development is incorporating perfectly matched layers (PML's), ports, and outgoing-wave boundary conditions.

CTLSS can be employed for solving diverse practical problems, such as the computation of electromagnetic fields developing in components for high-power microwave generation [e.g., klystrons, coupled-cavity and helix traveling wave tubes (TWT's), and gyroklystrons], including absorbing materials commonly used to control mode Q and to suppress spurious oscillations. Applications to particle accelerators include the simulation of microwave accelerator cavities, couplers, etc. Cavity eigenmode solutions provide mode frequencies, Q 's and eigenfields, as well as dispersion and coupling impedance. CTLSS has the capability for simultaneous extraction of all eigenmodes in a given band. Fig. 1 depicts several configurations to which CTLSS has been applied.

The electromagnetic solver in CTLSS has been designed to handle two separate classes of problems, resonant and nonresonant frequency-domain simulations. The nonresonant solver uses the "quasi-minimal residual" (QMR) method [5] to invert the linear matrix equation

$$\mathbf{A}x = b$$

where A is a very large matrix, and the problem therefore may best be solved using iterative methods. The QMR method offers

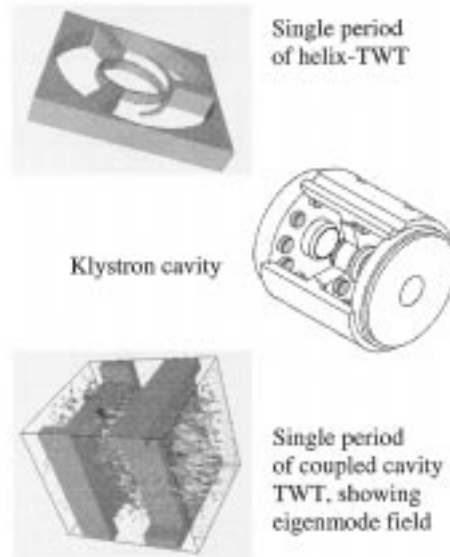


Fig. 1. Some electromagnetic applications of the CTLSS code.

the advantage that it works very well when A is non-Hermitian and, therefore, can handle problems with lossy materials.

The resonant eigenvalue problem involves the solution of the generalized eigenvalue equation

$$\{\mathbf{A} - \lambda_n \mathbf{B}\}x_n = 0$$

where both A and B are large matrices. CTLSS uses the Jacobi–Davidson method [6] to solve these problems. Jacobi–Davidson is a purely iterative method related to the Rayleigh quotient iteration (RQI) Method, and it uses a Block–Galerkin procedure for the estimation of eigenvalues. The subspace is updated via an approximate (iterative) linear solution [7], followed by subspace augmentation [8]. The original formulation of the Jacobi–Davidson algorithm [6] calculates a set of solutions in a given range, $\lambda_{\min} < \lambda_n < \lambda_{\max}$, and therefore can exclude static solutions automatically. It also obtains high-order mode solutions efficiently. The subspace update step uses the QMR algorithm to ensure stable behavior with lossy materials.

The Jacobi–Davidson model offers several advantages over other eigenvalue models as follows.

- 1) It handles lossy materials with high loss tangent (complex eigenvalues).
- 2) All modes are ensured to converge to the same specified level of accuracy—the unnecessary use of resources in converging additional modes is avoided.
- 3) The algorithm can start or restart with an approximate solution.
- 4) The algorithm can be accelerated using multilevel methods.

These features are described in the remainder of this paper. During the development of CTLSS, the Jacobi–Davidson algorithm was modified [9] to control the growth of the subspace during the solution. Additional modifications to accelerate convergence are described in Section V.

The large-signal model in CTLSS is currently based on the one-dimensional (1-D) CHRISTINE code [10] that was

developed for modeling helix TWT's. This model has been generalized first to provide a three-dimensional model, CHRISTINE-3D, for the helix TWT. The current development activity is aimed at the development of a general three-dimensional large-signal model, described in Section III.

II. ELECTROMAGNETIC THEORY AND NUMERICAL FORMULATION

CTLSS solves Maxwell's equations in three dimensions to obtain full electromagnetic solutions in the frequency domain for either the resonant eigenmodes or the driven-frequency response of an electromagnetic structure.

A. Maxwell's Equations—Continuum Theory

Maxwell's equations provide a continuum model, based on partial differential equations for the electric and magnetic fields in space and time. The equations describe the relationships of these fields to each other and their interaction with materials through a set of constitutive relations.

1) *Frequency Domain and Time Domain*: In the time domain, Maxwell's *curl* equations are written as

$$\begin{aligned}\text{curl } \vec{\mathbf{H}} &= \vec{\mathbf{J}} + \frac{\partial \vec{\mathbf{D}}}{\partial t} \\ \text{curl } \vec{\mathbf{E}} &= -\frac{\partial \vec{\mathbf{B}}}{\partial t}\end{aligned}$$

in terms of the electric field and displacement vectors $\mathbf{E}(\mathbf{x}, t)$ and $\mathbf{D}(\mathbf{x}, t)$, the magnetic field and flux density vectors $\mathbf{H}(\mathbf{x}, t)$ and $\mathbf{B}(\mathbf{x}, t)$, and the electric current density vector $\mathbf{J}(\mathbf{x}, t)$.

The linear constitutive relations

$$\begin{aligned}\vec{\mathbf{D}} &= \underline{\underline{\epsilon}} \vec{\mathbf{E}} \\ \vec{\mathbf{H}} &= \underline{\underline{\mu}}^{-1} \vec{\mathbf{B}}\end{aligned}$$

express the relationships between \mathbf{E} and \mathbf{D} and between \mathbf{B} and \mathbf{H} that are required to solve Maxwell's equations in either the time domain or the frequency domain. Bulk material properties are described by the permittivity and permeability tensors, $\underline{\underline{\epsilon}}$ and $\underline{\underline{\mu}}$.

To derive the frequency domain equations, the electric and magnetic fields and sources are assumed to be harmonic functions of time, using the convention

$$\vec{\mathbf{E}} = \text{Re}(\vec{\mathbf{E}} e^{-i\omega t}).$$

Substitution into Maxwell's equations then yields the frequency domain equations

$$\begin{aligned}\text{curl } \vec{\mathbf{H}} &= \vec{\mathbf{J}} - i\omega \vec{\mathbf{D}} \\ \text{curl } \vec{\mathbf{E}} &= i\omega \vec{\mathbf{B}}.\end{aligned}$$

Using the curl operation and the constitutive relations to eliminate all fields but E and J , these equations give the second-order vector differential equation

$$\left\{ \text{curl } \underline{\underline{\mu}}^{-1} \text{curl} - \omega^2 \underline{\underline{\epsilon}} \right\} \vec{\mathbf{E}} = i\omega \vec{\mathbf{J}}.$$

For a driven-frequency problem, a prescribed spatial distribution of \mathbf{J} at a specified value of ω drives the electric field solution. Then, these equations define a standard linear operator problem of the form $\mathbf{A}\mathbf{x} = \mathbf{b}$ that can be solved with appropriate boundary conditions to obtain the spatial profiles $E(\omega, \mathbf{r})$ that describe the electric field response to this source at the given frequency. If the system is driven on a resonance, very large amplitude solutions will be driven. The driven amplitude is proportional to the Q of the resonant mode. Solutions of this type are discussed in Section IV.

With no source field, J , this equation takes the standard form of a generalized eigenvalue problem of the form $\mathbf{A}\mathbf{x}_n = \lambda_n \mathbf{B}\mathbf{x}_n$, which describes the resonant modes of the structure

$$\left\{ \text{curl } \underline{\underline{\mu}}^{-1} \text{curl} - \omega_n^2 \underline{\underline{\epsilon}} \right\} \vec{\mathbf{E}}_n = 0$$

where normal-mode frequency squared ω^2 is the eigenvalue of the system, associated with the electric field eigenvector. Eigenvalue solutions are discussed in Section V.

To handle arbitrary coordinate systems, we express Maxwell's equations in tensor form

$$\begin{aligned}\epsilon^{ijk} \frac{\partial H_k}{\partial x^j} &= j^i + \dot{D}^i \\ \epsilon^{ijk} \frac{\partial E_k}{\partial x^j} &= -\dot{B}^i\end{aligned}$$

in terms of a set of global logical coordinates, $(\bar{x}^1, \bar{x}^2, \bar{x}^3)$. The global physical Cartesian coordinates $(x^1, x^2, x^3) \equiv (x, y, z)$ are expressed as a mapping from the logical coordinates from which the metric g_{ij} is obtained, i.e., where

$$\begin{aligned}x^i &= x^i(\bar{x}^1, \bar{x}^2, \bar{x}^3) \\ (g^{1/2} \epsilon^{ijk}) &= e^{ijk} \equiv \begin{cases} 1, & \text{for cyclic indexes} \\ 0, & \text{with repeated index} \\ -1, & \text{for anticyclic indexes} \end{cases} \\ g &= \det g_{ij}, \quad i, j, k \in \{1, 2, 3\}.\end{aligned}$$

The logical coordinate domain chosen for our discretization is a 3-D grid of unit, cubic cells, for which the numerical computation is greatly simplified, mapped to a physical domain that may be nonuniform, curvilinear, and even nonorthogonal.

The equations may be transformed into a simpler, metric-free form by a volumetric scaling of parameters [11]

$$\begin{aligned}e^{ijk} \frac{\partial H_k}{\partial \bar{x}^j} &= I^i + d^i \\ e^{ijk} \frac{\partial E_k}{\partial \bar{x}^j} &= -b^i\end{aligned}$$

where

$$\begin{aligned}d^i &= g^{1/2} D^i \\ b^i &= g^{1/2} B^i \\ I^i &= g^{1/2} j^i.\end{aligned}$$

This prescription permits the metric information to be amalgamated with the anisotropic, continuum materials parameters when the physical problem is mapped into logical coordinates.

Although the tensor constitutive relations in the physical space are written as

$$\begin{aligned} D_i &= \varepsilon_i^j E_j \\ H_i &= (\mu^{-1})_i^j B_j \end{aligned}$$

they may be expressed in the logical space as

$$\begin{aligned} d^i &= C^{ij} E_j \\ H_i &= L_{ij}^{-1} b^j \end{aligned}$$

where

$$\begin{aligned} C^{ik} &= g^{1/2} g^{ij} \varepsilon_j^k \\ L_{ik}^{-1} &= g^{-1/2} g_{ij} (\mu^{-1})_k^j. \end{aligned}$$

In the dimensionless logical coordinate system, the tensors C^{ij} and L^{ij} have units of capacitance and inductance, respectively, E has units of voltage, d has units of charge, b has units of magnetic flux, and H has units of current. The simple form of the continuum equations obtained makes the discretization procedure required for a numerical solution particularly straightforward. This procedure is detailed in Section II-B.

2) *Material Properties:* The model described above readily includes ideal materials, such as loss-free dielectrics and perfect metals. The modeling of vacuum electron devices requires the inclusion of real materials that often are employed to control the device behavior. Material properties currently implemented in CTLSS include the following.

a) *Complex (lossy) materials:* These materials have complex values of ε and μ , which are required for simulating energy losses in the material. In the equations above, when the materials can have complex properties, the field solutions also become complex. The major complication that develops is that the resulting operator is non-Hermitian, in general, and common solution methods fail. Algorithms for handling such operators are described in Sections IV and V.

b) *Resistive materials:* The equations above generalize to include Ohmic losses by writing the current density as $\mathbf{J} = \mathbf{J}_s + \mathbf{J}_\Omega$, and expressing the Ohmic current density as $\mathbf{J}_\Omega = \boldsymbol{\sigma} \cdot \mathbf{E}$ to obtain

$$\left\{ \text{curl } \underline{\underline{\mu}}^{-1} \text{curl} - i\omega \underline{\underline{\sigma}} - \omega^2 \underline{\underline{\varepsilon}} \right\} \vec{E} = i\omega \vec{J}_s$$

which yields an operator that is quadratic in ω .

An approximate treatment of this equation is usually employed, in which a complex permittivity

$$\underline{\underline{\tilde{\varepsilon}}} = \underline{\underline{\varepsilon}} + \frac{i\underline{\underline{\sigma}}}{\omega}$$

is defined, and then assumed to be independent of ω , so that the operator again becomes linear in ω^2

$$\left\{ \text{curl } \underline{\underline{\mu}}^{-1} \text{curl} - \omega^2 \underline{\underline{\tilde{\varepsilon}}} \right\} \vec{E} = i\omega \vec{J}_s.$$

This approximation usually can be justified over a narrow range of frequencies.

c) *Anisotropic materials:* The formulation above permits treatment of the full tensor equations for materials having

3×3 tensor material properties ε_{ij} and μ_{ij} . At present, the discretization method implemented in CTLSS supports only diagonal tensor material properties, although this is not an inherent limitation of the method. Diagonal tensor properties are simpler because each of the diagonal tensor components is associated with a single field component (e.g., $D_x = \varepsilon_{xx} E_x$), and the resulting matrix equations are simplified.

It is sometimes impractical or impossible to align the coordinate system in a simulation with the principal axes of the anisotropic material, and the ability to treat the full 3×3 tensor is therefore required in such cases. As described above, the 3×3 permittivity tensor can be combined with the 3×3 metric tensor describing a nonorthogonal grid to include both effects without requiring additional storage. Using this feature, anisotropic dielectrics can be automatically included within a nonorthogonal grid formulation. This capability is presently under development.

d) *Dispersive materials:* These are materials having frequency-dependent material properties $\varepsilon(\omega)$ and $\mu(\omega)$. All lossy materials must be dispersive because the imaginary part of $\varepsilon(\omega)$ and $\mu(\omega)$ must be odd functions of frequency whenever the real part is an even function.

A model for dispersive materials that is valid for several ceramic materials and for cold plasma is based on writing the permittivity as

$$\tilde{\varepsilon} = \tilde{\varepsilon}_{[0]} \left(1 - \frac{\omega_p^2(\vec{x})}{\omega^2} \right)$$

where ω_p^2 depends on position and yields the modified operator

$$\left\{ \left[\text{curl } \underline{\underline{\mu}}^{-1} \text{curl} + \omega_p^2(\vec{x}) \underline{\underline{\tilde{\varepsilon}}}_{[0]} \right] - \omega^2 \underline{\underline{\tilde{\varepsilon}}}_{[0]} \right\} \vec{E} = i\omega \vec{J}_s.$$

3) *Boundary Conditions:* Boundary conditions (BC's) typically define or limit the efficacy of simulation tools. The following types of boundary conditions are particularly useful in electromagnetic simulation codes.

a) *Electric wall:* This BC represents a type of symmetry plane in which the wall acts as a perfect conductor. In this case, the tangential electric field and the normal magnetic field at the wall are zero.

b) *Magnetic wall:* This BC is the complement of the electric wall, with the tangential magnetic field and normal electric field components zero.

c) *Floquet boundary:* The Floquet BC is a periodic boundary condition having a specified phase advance across the period. To impose a phase advance θ across a period L in z , the boundary condition is

$$\vec{E}(x, y, L) = \vec{E}(x, y, 0) e^{i\theta}.$$

It is used to simulate many periodic field solutions using only a well-resolved period of the structure. As special cases, phase-angles of 0° and 180° require only the real-valued factors ± 1 .

d) *Impedance wall:* This type of BC allows surface impedances to be used in place of modeling the actual volume of a lossy material. Typically, such boundaries are used to simulate thin coatings on metallic surfaces or as a model for open

absorbing boundaries. The form of the impedance function depends on the material and structure that it represents. Typically, the impedance is dispersive; i.e., it is a function of frequency.

The impedance wall BC is most often used in two situations: 1) to model a resistive metal whose thickness is many skin depths, and 2) to model a thin resistive coating (with thickness less than a skin depth) on a perfectly conducting substrate. The boundary condition is founded on Ohm's law

$$\vec{E}_{\text{tan}}(\vec{r}) = Z_s(\vec{r}, \omega) \vec{J}_{\text{surface}}(\vec{r}) = Z_s(\vec{r}, \omega) [\hat{n} \times \vec{H}(\vec{r})]$$

where Z_s is the surface impedance and \hat{n} is the surface normal. This expression is used to update the tangential electric field E from H at the boundary.

e) Radiating or open boundary: This BC matches electromagnetic waves at the boundary to outgoing radiation fields so that the boundary acts as though it were not there and generates no reflected waves. Lindman [12] has described the implementation of open, radiating BC's for the discrete wave equation by using projection operators to simulate an infinite region of free space in contact with the computational region.

f) Ports: A variation of the open BC is the "port." Port BC's are models that match outgoing waves into an aperture as though that aperture is the entrance to an infinitely long waveguide. The fields in the aperture are decomposed into waveguide modes, and each component is matched to waveguide modes having the same phase velocity as the incident wave.

g) Perfectly matched layer (PML): The PML is a method of using impedance boundaries to simulate the impedance of free space. It is an alternative to the open BC described above. In practice, a single-layer impedance BC can match perfectly only for waves over a narrow band of incident angles. By constructing the impedance from multiple layers, however, the boundary can be designed to match outgoing waves over a broad range of angles. The PML is usually implemented as a volumetric resistive layer, extending over 4–30 cells for good matching, and it is therefore not strictly a boundary condition. The PML implementation is described in Section II-B5.

h) Far-field transform: This boundary condition transforms the near-field solution at a radiating boundary into the far field so that radiation patterns can be computed without carrying out large simulations. This capability is particularly important for radiating elements such as antennas. By decomposing the outgoing waves on a close-in surface into spherical multipole components, we can analytically carry the solution to the far field.

i) External circuit: Another specialization of the surface impedance BC is the external circuit BC. In this case, the impedance condition is set from an external model, typically a lumped circuit or a transmission line model, relating the electric and magnetic fields at the boundary.

B. Maxwell's Equations—Discrete Theory

Numerous numerical methods [13] have been developed to approximate the solution of the continuum Maxwell's equations. These methods divide approximately into two broad classes: surface methods and volume methods. In surface

methods, the boundaries of all surfaces in the problem are discretized, and a superposition of Green's function solutions from each surface element is used to compute the electromagnetic fields everywhere in the enclosed volume. This method works well when there are few embedded structures or volume materials and when the scale of the simulation is no more than a few wavelengths. Volume methods, which are the focus of this paper, involve gridding the entire volume of the simulation and discretizing Maxwell's equations throughout the solution domain.

1) Finite Integration Theory (FIT): The discretization of Maxwell's equations is based on an orthogonal, structured grid model, which has been implemented in the CTLSS code. The methodology generalizes readily to a nonorthogonal, structured grid model, which is planned in a future CTLSS release, and which will allow embedded structures to be treated with conformal coordinates. In the current implementation, a continuous mapping is used to include non-Cartesian coordinates, such as cylindrical coordinates, which allow certain problems to be executed with greater accuracy and fewer computational cells.

Before discretizing, we construct a $N^1 \times N^2 \times N^3$ grid of cubic cells as the logical coordinate system, with coordinates $\vec{x}^i \in [0, N^i]$, and define a continuous, piecewise-linear mapping to the physical space by interpolating among sets of control points. For cylindrical geometry, the mapping is made first to global cylindrical coordinates, (r, θ, z) . Then, a continuous transformation is used to map (r, θ, z) to Cartesian coordinates, (x, y, z) , with special attention to handle on-axis singular points.

The physical model is cast in the logical space, where each cell is a simple unit cube. In the logical coordinate system, the metric-free differential equations are used, the continuous electric field vector has dimensions of voltage, and the other field quantities are expressed similarly as their analogous circuit quantities, defined earlier.

The discretization procedure is similar to that of the finite integration technique (FIT) [14], [15]. Field quantities are associated with the edges and faces of the grid cells, using the now standard Yee-cell arrangement [16]. This arrangement actually consists of two interleaved grids. On one grid, the components of the \mathbf{E} vector are defined on the cell edges parallel to that component, and the components of the \mathbf{B} vector are defined at the centers of the cell faces orthogonal to that component. In the FIT, the discrete fields are stored as cell voltages \mathbf{V} on each edge of the cell and magnetic fluxes Φ through each cell face. The cell currents \mathbf{I} are stored on the dual-cell edges, and the electric displacement fluxes \mathbf{Q} through the dual-cell faces. The constitutive relations then relate \mathbf{Q} and \mathbf{V} through the cell capacitance matrix D_C and Φ and \mathbf{I} through the cell inductance matrix D_L .

The inductance and capacitance matrices account for the cell geometry as well as the average permittivity and permeability tensors for that field component. If the permittivity and permeability tensors are diagonal and the coordinate system is orthogonal, D_C and D_L are diagonal matrices.

The differential operators derive from the integral forms of Maxwell's equation and involve directed summations of adjacent field quantities. The *curl* operator evaluated for the face of

a grid cell is a simple, directed sum corresponding to the line integral around the face edges. This operator may be represented as a matrix operator \hat{c} , though this matrix is never formed explicitly. The matrix representation for the curl on the dual grid cell is simply the transpose \hat{c}^T [15].

The FIT technique provides a means to create a discrete matrix equation from the continuum field equations. It offers the following advantages:

- a) The method is readily generalized to a related finite element (FE) method.
- b) Maxwell's equations and field variables map to familiar electrical circuit quantities.
- c) Differential operators translate to very sparse matrices, having only element values, 0 and ± 1 , that are fast to compute.
- d) The structured grid permits fast matrix-vector products.
- e) All differential operator identities are satisfied.
- f) The coordinate metric is incorporated with material parameters.
- g) Symmetries in the original equations are retained.

2) *Treatment of Materials:* Materials are treated through the inductance and capacitance tensors, described above. These tensors include all of the geometry and materials data for each cell, and for orthogonal grids, the discrete diagonal matrix elements are defined as integrals over the relevant tensor component

$$D_C^{(j)} = \iint_{\tilde{A}_j} C^{ii} d^2x$$

$$D_L^{(j)-1} = \iint_{\tilde{l}_j} L_{ii}^{-1} dx$$

where integration is over the face and edge, respectively, \tilde{A}_j and \tilde{l}_j , of the logical dual grid at the location of the corresponding field element j , having direction i . Each integral is calculated by numerical integration, summing contributions from each adjacent cell.

Maxwell's equations and the constitutive relations then carry over to circuit equations

$$\text{curl } \vec{H} = \vec{J} - i\omega \vec{D} \Rightarrow \hat{c}^T \vec{I} = \vec{I}_s - i\omega \vec{Q}$$

$$\text{curl } \vec{E} = i\omega \vec{B} \Rightarrow \hat{c}V = i\omega \Phi$$

and

$$\vec{D} = \epsilon \vec{E} \Rightarrow \vec{Q} = D_C V$$

$$\vec{H} = \mu^{-1} \vec{B} \Rightarrow \vec{I} = D_L^{-1} \Phi$$

where quantities on the dual grid have been denoted by " \sim ."

3) *Matrix Formulation:* The linear eigenvalue operator equation

$$\left\{ \text{curl } \underline{\mu}^{-1} \text{curl} - \omega_n^2 \underline{\epsilon} \right\} \vec{E}_n = 0$$

is implemented in CTLSS as the matrix equation

$$\left\{ (\hat{c}^T D_L^{-1} \hat{c}) - \omega_n^2 D_C \right\} V_n = 0.$$

The matrix size, $3N \times 3N$, where $N = N^1 N^2 N^3$, can be enormous in 3-D problems. Typically, $3N$ is $\sim 10^5$ – 10^6 , but the matrices are usually sparse, requiring storage of $O(3N)$ elements.

CTLSS solves the matrix equation iteratively, using an operator function to compute the differential operator matrix elements "on the fly," as needed. It does not store the matrix explicitly. Where possible, matrix symmetry can be employed to reduce the calculations by half.

This matrix equation takes the form of a generalized matrix eigenvalue problem

$$Ax_n = \lambda_n Bx_n.$$

Several distinct classes of problems emerge as follows.

- a) Without Ohmic losses, and using only electric-wall, magnetic-wall, or Floquet BC's, the problem is Hermitian; i.e., $A = A^H$ and $B = B^H$. In this case, the eigenvalues are real and the eigenvectors are orthogonal.
- b) With Ohmic losses, and using only electric-wall, magnetic-wall, or simple periodic BC's, the problem is complex symmetric; i.e., $A = A^T$ and $B = B^T$. In this case, the eigenvalues are complex and the eigenvectors are linearly dependent.
- c) With both Ohmic losses and Floquet BC's, the problem is both non-Hermitian and nonsymmetric.

The eigenvalue problem has the troublesome property that it admits static solutions, having *curl*-free eigenvectors and zero eigenvalue, $\omega = 0$. Such solutions must be carefully avoided or eliminated. CTLSS avoids static solutions by forcing the solver to seek solutions within a prescribed frequency band. Other codes employ a "penalty function" to constrain the operator away from zero-*curl* solutions.

4) *Treatment of Simple Boundary Conditions:* A particular problem is completely defined by the material parameters over a domain, the domain shape, and the field boundary conditions at the domain boundary. The solution is then obtained in some coordinate system, either orthogonal (e.g., Cartesian, cylindrical, etc.) or nonorthogonal (having a nondiagonal metric).

At present, the CTLSS model for orthogonal coordinates includes the most commonly used, and useful, boundary conditions, as follows.

- a) Electric wall (or metal wall)

$$\hat{n} \times \vec{E} = 0, \quad \hat{n} \cdot \vec{B} = 0.$$

Electric fields on the boundary of a metallic cell are set to zero.

- b) Magnetic wall (or symmetry)

$$\hat{n} \times \vec{H} = 0, \quad \hat{n} \cdot \vec{D} = 0.$$

This is the natural boundary condition, and it requires that the capacitance and inductance integrals be restricted to the solution domain.

- c) Floquet (or periodic with phase advance)

$$\vec{E}(\vec{r}_0 + \vec{\delta}r) = \vec{E}(\vec{r}_0) \exp(i\vec{\beta} \cdot \vec{\delta}r).$$

Electric fields at one face of the solution domain are set to equal those at the opposite face, scaled by the complex exponential phase factor.

5) *Perfectly Matched Layer (PML):* For an outgoing wave boundary condition, CTLSS implements a PML [17]. In this

model, the boundary surface is extended to a volumetric layer containing an artificial absorbing material having a particular inhomogeneous distribution of anisotropic material parameters. The parameters are chosen such that the transition for an incident wave is well matched and waves are almost perfectly absorbed over a wide range of frequencies and incident angles. Our implementation is related to the stretched coordinate formulation of that method [18], [19], but it is derived by a generalized metric tensor. This technique derives from the complex-coordinate method [20] using *exterior scaling* [21], [22], extended to apply to vector fields in three dimensions.

The complex-coordinate method expresses a set of differential equations over a domain in which the coordinates are not constrained to be real valued, but may follow a continuous trajectory in the complex plane. The solution of the equations may be found on this domain, and related to the solution over the real domain by analytic continuation. Typically, the complex-coordinate trajectories are chosen to follow the real axis over most of the solution volume of interest, but they deviate increasingly once outside of this region. Such a domain may be open, in the sense that the complex-coordinate trajectory is infinite in extent, but for numerical computation, it will be terminated at a finite distance.

The differential equations take their usual form where the coordinates are real, and they are therefore modified only in the bounding region, such that they represent a modified volumetric boundary condition. The effective properties of this complex-coordinate boundary region are such that a propagating wave gradually transforms into an exponentially decaying wave. Therefore, if the numerical grid extends sufficiently far into the complex-coordinate region, the outgoing wave will effectively vanish, and termination of the numerical grid will have no significant influence on the solution in the region of interest. It therefore acts as an effective outgoing wave boundary condition.

In our implementation, the components of the metric tensor are derived assuming only that the mapping from the logical coordinates to the global coordinates is to the complex-coordinate system. PML regions correspond to zones where one or more coordinates have a nonzero imaginary component. This gives us a uniform treatment that allows us to include the PML into the complex capacitance and inductance matrices without modifying the actual material properties. Properties such as loss or anisotropy are therefore carried over directly into our PML formulation automatically without additional consideration.

III. LARGE-SIGNAL THEORY FORMULATION

A full 3-D treatment of the beam-wave interaction is essential if we need to compute quantities like circuit interception current or transverse beam exit distributions that are unavailable from a 1-D code for linear beam tubes. The CTLSS code will be able to analyze the 3-D interactions of an electron beam with an arbitrary surrounding structure. In order to do so, the code must take into account three distinct types of fields when computing the motion of the beam and the evolution of the RF signals of interest. These are 1) the externally applied focusing field, 2) the structure field, and 3) the space charge field.

The focusing field is generally a DC magnetic field produced by coils or permanent magnets positioned near the beam. 1-D treatments of beam-wave interactions assume that the transverse focusing strength of these fields is so large that transverse beam motion may be neglected. Such codes, therefore, do not need any quantitative information about the focusing fields—they are assumed to be “infinitely strong.” Full 3-D codes, like CTLSS, however, must import some representation of the actual fields, generally from another code like POISSON/PANDIRA [23], [47], MAXWELL (product of Ansoft Corporation), mPPM [24], or lesPPM [25]. Below, we will assume that these fields are available in some form to the simulation and we will not say much more about them.

The structure fields are produced by charges moving on the surfaces of the metallic structure surrounding the beam. These fields are solutions to Maxwell’s equations in vacuum, with the appropriate boundary conditions on the surface of the circuit. There are two basic types of structure used in linear beam tubes. One is a traveling-wave structure, composed of a series of many, nearly identical unit cells, as in TWT’s or backward wave oscillators. The other is composed of a series of a small number of generally nonidentical resonant cavities that do not share energy, except as carried by the beam, as in klystrons.

The large-signal model currently linked to CTLSS is the CHRISTINE code [10], a 1-D large-signal code for helix TWT’s. CHRISTINE 3-D is an extension of CHRISTINE to handle 3-D helix TWT configurations, and it will be linked to CTLSS in the near future. A generalization of CHRISTINE 3-D to handle devices other than helix TWT’s is “future development” work. The large signal algorithm in CTLSS will be designed initially to treat the interactions of an electron beam with traveling waves supported by a periodic, slow-wave structure. The interaction may be with either forward or backward waves, as described below.

Traveling waves are characterized by their dispersion relation (relation between frequency and wavelength) and by their interaction impedance (field strength per unit power). In one dimension, when the only structure field of interest is the longitudinal electric field, it suffices to specify only phase velocity and interaction impedance for each signal frequency. In three dimensions, as we shall see, when all components of both the RF electric and magnetic fields must be included, additional information is required to compute the full set of structure fields in the interaction region.

The space charge fields, produced by the neighboring charges in the beam, are generally the most difficult to treat, because the full set of Maxwell’s equations must be solved, using the beam current and charge density as the source terms, subject to suitable boundary conditions on the circuit surface. Care must be taken not to double count the structure fields, whose strength is also proportional to beam current, when computing the space charge fields.

The large signal algorithm under development for CTLSS is a generalization of the one used in the 3-D helix TWT code, CHRISTINE 3-D, which uses analytical models for the sheath and tape [26] helix. CHRISTINE 3-D is, and CTLSS will initially be, a multifrequency, steady-state code, in which all quantities are assumed to oscillate at a set of specified, real-valued

signal frequencies. These frequencies must all be integer multiples of some lowest frequency, in order that certain time averages may be calculated. There is no other explicit time dependence, however. All quantities, including particle location (phase) and momentum and field amplitudes and phases, are integrated along the direction of beam propagation. The full set of equations governing the evolution of the particles and the fields is derived below.

A. The Structure Fields and Their Evolution

We consider the waves supported by an arbitrary periodic structure composed of metal and dielectric. As in [10], hereafter referred to as A-L, where the analysis is specialized to a helix circuit, the solutions to Maxwell's equations may be written in the generalized Floquet form

$$\mathbf{E}_{rf}(\mathbf{x}, t) = \sum_{\omega} i \frac{\omega}{c} A_{\omega} \mathbf{e}_{\omega}(\mathbf{x}) \cdot \exp \left[i \left(\int_0^z k_{z\omega}(z') dz' - \omega t \right) \right] + \text{c.c.} \quad (1)$$

$$\mathbf{B}_{rf}(\mathbf{x}, t) = \sum_{\omega} i \frac{\omega}{c} A_{\omega} \mathbf{b}_{\omega}(\mathbf{x}) \cdot \exp \left[i \left(\int_0^z k_{z\omega}(z') dz' - \omega t \right) \right] + \text{c.c.} \quad (2)$$

where $\mathbf{E}_{rf}(\mathbf{x}, t)$ and $\mathbf{B}_{rf}(\mathbf{x}, t)$ are the electric and magnetic fields and $\mathbf{e}_{\omega}(\mathbf{x})$ and $\mathbf{b}_{\omega}(\mathbf{x})$ are dimensionless solutions to Maxwell's equations for frequency ω and propagation constant $k_{z\omega}$. We will take $k_{z\omega}$ to be real; circuit attenuation will be accounted for separately; see below. To allow for slow axial variation (tapering) of the slow-wave structure, the propagation constant $k_{z\omega}$ is taken to vary slowly with axial distance. The functions $\mathbf{e}_{\omega}(\mathbf{x})$ and $\mathbf{b}_{\omega}(\mathbf{x})$ are periodic with the local structure period; these are obtained from the solutions by the CTLSS cold test module. A_{ω} is the field amplitude; it has units of vector potential (gauss-cm). In the presence of the beam it too will be taken to vary slowly with z . The sums in (1) and (2) are over a discrete set of real frequencies ω , all of which are assumed to be integer multiples of a lowest frequency ω_0 . CGS units are used.

For a specified frequency ω , which we take to be a positive real number, $k_{z\omega}$ is determined by the CTLSS code test module. If $k_{z\omega}$ is a root of the dispersion relation, so are $(\pm k_{z\omega} + nk_s)$, where $k_s \equiv 2\pi/L_s$ is the wavenumber corresponding to the structure period L_s and n is any integer. Without loss of generality, we take $|k_{z\omega}| \leq \pi/L_s$.

According to common convention, all periodic structures are classified as either forward wave or backward wave, according to whether the slope of the $\omega - k_{z\omega}$ relation in the region $0 < k_{z\omega} < k_s/2$ is positive or negative, respectively. Examples are shown in Figs. 2 and 3. In each case, spatial harmonics with positive group velocity (energy flow in the $+z$ direction) are shown as solid lines and spatial harmonics with negative group velocity are shown as dashed lines. A signal injected at $z = 0$ and propagated toward a load at $z = z_L > 0$ has positive group velocity by this definition; it is composed of a superposition of all spatial harmonics shown as solid lines in Fig. 2. If we always define the direction of beam propagation to be $+z$, in forward

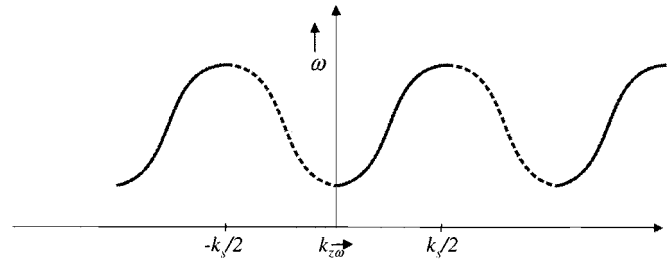


Fig. 2. Dispersion relation for a forward wave structure.

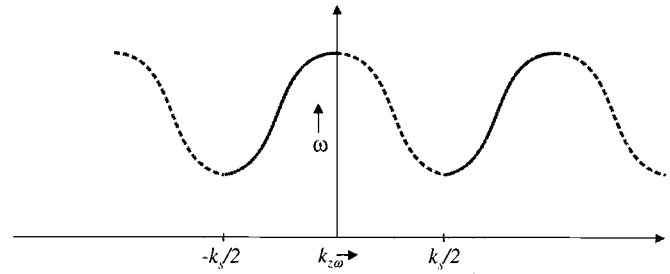


Fig. 3. Dispersion relation for a backward wave structure.

wave structures, the group velocity of the injected signal must also be in the $+z$ direction and in backward wave structures, the group velocity must be in the $-z$ direction. Note that if in a forward wave structure the injected signal is partially reflected from a circuit termination or imperfection, the reflected wave will have negative group velocity; a spatial harmonic of the reflected wave (dashed lines of Fig. 2) may also interact with the beam.

The power flowing along the structure may be obtained by substituting (1) and (2) into the expression for the Poynting flux. The result is

$$P = P_0 \sum_{\omega} |a_{\omega}(z)|^2 \equiv \sum_{\omega} P_{\omega} \quad (3)$$

where the normalized wave amplitude has been defined as

$$a_{\omega}(z) = \frac{\omega}{c} \frac{q A_{\omega}}{m c^2} A_{\text{eff},\omega}^{1/2} \quad (4)$$

and

$$P_0 \equiv \frac{c}{2\pi} \left(\frac{m c^2}{q} \right)^2 = 1.386 \times 10^{16} \text{ ergs/s} \\ = 1.386 \times 10^9 \text{ W.} \quad (5)$$

An effective area of the mode has been defined in (4) as

$$A_{\text{eff},\omega} = \frac{1}{2} \int d^2x_{\perp} \hat{z} \cdot (\mathbf{e}_{\omega}^* \times \mathbf{b}_{\omega} + \mathbf{e}_{\omega} \times \mathbf{b}_{\omega}^*). \quad (6)$$

The integral in (6) is over the entire plane transverse to the z -axis. In (4) and (5), q and m are the electron charge and mass, and c is the speed of light in vacuum. In the following, we will drop the subscript ω .

If we consider the fields within an imaginary cylinder centered on the z -axis, but not intersecting any part of the slow-wave structure (See Fig. 4), the functional forms of $\mathbf{e}(\mathbf{x})$ and $\mathbf{b}(\mathbf{x})$ may be simply expressed in cylindrical coordinates.

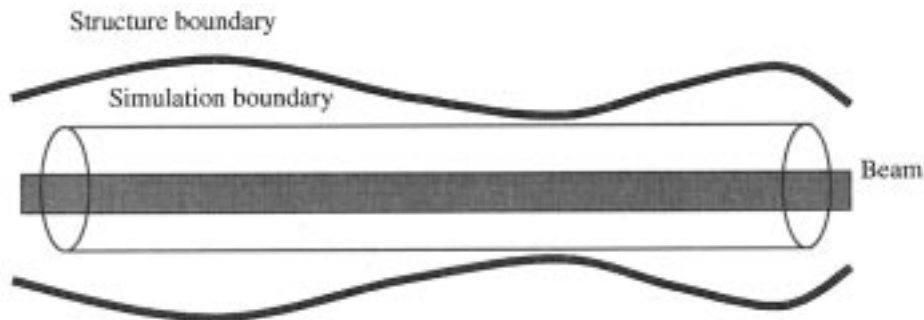


Fig. 4. Equations (7a) and (b) hold in cylindrical region bounded by the “simulation boundary,” the cylinder of largest radius that does not intersect the structure.

In particular, if we write the z -components of the normalized fields as

$$e_z(r, \theta, z) = \sum_{m=-\infty}^{\infty} \sum_{n=-\infty}^{\infty} e_{zmn}(r) \cdot \exp[-im\theta + ink_s z] \quad (7a)$$

$$b_z(r, \theta, z) = \sum_{m=-\infty}^{\infty} \sum_{n=-\infty}^{\infty} b_{zmn}(r) \cdot \exp[-im\theta + ink_s z] \quad (7b)$$

where $k_s = 2\pi/L_s$ is the wavenumber corresponding to the structure period, L_s , then the transverse components follow from Maxwell’s equations:

$$\gamma_n^2 e_{rnm}(r) = -ik_n \frac{\partial}{\partial r} e_{zmn}(r) - \frac{m}{r} \frac{\omega}{c} b_{zmn}(r) \quad (8a)$$

$$\gamma_n^2 e_{\theta mn}(r) = -\frac{m}{r} k_n e_{zmn}(r) + \frac{i\omega}{c} \frac{\partial}{\partial r} b_{zmn}(r) \quad (8b)$$

$$\gamma_n^2 b_{rnm}(r) = \frac{m}{r} \frac{\omega}{c} e_{zmn}(r) - ik_n \frac{\partial}{\partial r} b_{zmn}(r) \quad (8c)$$

$$\gamma_n^2 b_{\theta mn}(r) = -i \frac{\omega}{c} \frac{\partial}{\partial r} e_{zmn}(r) - \frac{m}{r} k_n b_{zmn}(r) \quad (8d)$$

where

$$k_n \equiv k_z + nk_s \quad (9)$$

and the radial propagation factor is defined by

$$\gamma_n^2 \equiv k_n^2 - \frac{\omega^2}{c^2}. \quad (10)$$

The axial components of the fields have simple representations in any region containing the origin. These are

$$e_{zmn}(r) = e_{zmn}^{(0)} I_m(\gamma_n r) \quad (11a)$$

$$b_{zmn}(r) = b_{zmn}^{(0)} I_m(\gamma_n r) \quad (11b)$$

where $e_{zmn}^{(0)}$ and $b_{zmn}^{(0)}$ are constants and $I_m(x)$ is the modified Bessel function of order m . $e_{zmn}^{(0)}$ may be expressed by the interaction impedance of the mode defined at some reference radius r_0 , defined as

$$K_{mn}(r_0) \equiv \frac{\left| 2 \frac{\omega}{c} A_\omega e_{zmn}(r_0) \right|^2}{2k_n^2 P_\omega} = \frac{4\pi}{c} \frac{|e_{zmn}(r_0)|^2}{k_n^2 A_{\text{eff}}} \quad (12)$$

still in CGS units. The extra factor of 2 in the numerator is from the definition of the fields as a sum of a quantity and its complex conjugate in (1) and (2). It follows that

$$A_{\text{eff}}^{-1/2} |e_{zmn}^{(0)}| = \frac{k_n}{I_m(\gamma_n r)} \left(\frac{K_{mn}(r_0)}{4\pi/c} \right)^{1/2}. \quad (13)$$

These impedances are simply calculated by the CTLSS code test module. Once it is known, the axial normalized electric field $A_{\text{eff}}^{-1/2} |e_{zmn}(r)|$ is known for all r , using (11a).

In order to obtain the transverse fields from (8d), for use in the 3-D equations of motion, it is necessary to know the axial magnetic field as well. To this end, it is convenient to define a quantity analogous to K_{mn} for the magnetic field

$$L_{mn}(r_0) \equiv \left(\frac{c}{4\pi} \right)^2 \frac{\left| 2 \frac{\omega}{c} A_\omega b_{zmn}(r_0) \right|^2}{2k_n^2 P_\omega} = \frac{c}{4\pi} \frac{|b_{zmn}(r_0)|^2}{k_n^2 A_{\text{eff}}} \quad (14)$$

where we have introduced the factor $(c/4\pi)^2$ to give L_{mn} the dimensions of admittance. The L_{mn} may also be simply calculated by the CTLSS code test module. It follows that

$$A_{\text{eff}}^{-1/2} |b_{zmn}^{(0)}| = \frac{k_n}{I_m(\gamma_n r)} \left(\frac{L_{mn}(r_0)}{c/4\pi} \right)^{1/2} \quad (15)$$

which, with (1), (7), (8), (12)–(14), give the structure fields everywhere in the beam.

It remains only to find the equation governing the evolution of the normalized mode amplitude $a_\omega(z)$ as the wave interacts with the beam. The development of this equation follows the standard derivation of Poynting’s theorem, as shown in A-L. The general result is

$$\begin{aligned} & \left(\frac{d}{dz} + \alpha(z) \right) a_\omega(z) \\ &= \frac{2\pi i}{I_A A_{\text{eff}}^{1/2}} \left\langle \int d^2 x_\perp \mathbf{J}(\mathbf{x}, t) \cdot e^*(\mathbf{x}) \right. \\ & \quad \left. \cdot \exp \left[-i \left(\int_0^z k_z(z') dz' - \omega t \right) \right] \right\rangle_{t,z} \quad (16) \end{aligned}$$

where $\alpha(z)$ is the attenuation per unit length, I_A is the Alfvén current (mc^3/q), $\mathbf{J}(\mathbf{x}, t)$ is the beam current density, and the angular brackets denote averages over the temporal period of the radiation and the spatial period of the structure.

We now write the current density as a sum over particles (instead of a sum over disks, as in A-L),

$$\mathbf{J}(\mathbf{x}, t) = \sum_k q_k \mathbf{v}_k(t) \delta^{(2)}(\mathbf{x}_\perp - \mathbf{x}_{\perp k}(t)) \delta(z - z_k(t)) \quad (17)$$

where q_k is the charge, $\mathbf{x}_k(t) = (\mathbf{x}_{\perp k}(t), z_k(t))$ is the position at time t , and $v_k(t)$ is the velocity of particle k at time t . Substituting (17) into (16) and performing the integrals over \mathbf{x}_\perp and t gives, for the right hand side of (16)

$$\frac{2\pi i}{I_A} \sum_{k \in T} I_k \left\langle \frac{\mathbf{v}_k(z) \cdot \mathbf{e}^*(\mathbf{x}_k(z))}{v_{zk}(z) A_{\text{eff}}^{1/2}(z)} \cdot \exp \left[-i \left(\int_0^z k_z(z') dz' - \omega t_k(z) \right) \right] \right\rangle_z \quad (18)$$

where the sum is now over all particles that enter during an RF period, T , $I_k = q_k/T$ is the current associated with ‘‘beamlet’’ k , and all particle positions and velocities are now functions of z ; $t_k(z)$ is the arrival time of particle k at z . In order to perform the remaining average in z , over a structure period L_s , we expand the electric field as in (7), to obtain

$$\frac{2\pi i}{I_A} \sum_{k \in T} \sum_{m,n} I_k \left\langle \frac{\mathbf{v}_k(z) \cdot \mathbf{e}_{mn}^*(r_k)}{v_{zk} A_{\text{eff}}^{1/2}} \cdot \exp \left[-i \left(-m\theta_k(z) + \int_0^z k_n(z') dz' - \omega t_k(z) \right) \right] \right\rangle_z. \quad (19)$$

If we assume that the transverse particle position and velocity do not change much within a structure period, the only term in the sum over n in (19) that will survive the averaging process over z is a term for which

$$\omega \approx k_n v_{z0} \quad (20)$$

for some value of n . This clearly means just that the beam is synchronous with the n th spatial harmonic of the wave. Linear beam tubes are generally designed to satisfy (20) for $n = 0$ or 1 , because the interaction impedance K_{mn} typically decreases with increasing values of n .

We denote the index of the synchronous spatial harmonic as n_s and write

$$\int_0^z k_{n_s}(z') dz' - \omega t_k(z) \equiv \int_0^z \left(k_{n_s}(z') - \frac{\omega}{v_{z0}} \right) dz' + \omega \left(\frac{z}{v_{z0}} - t_k(z) \right). \quad (21)$$

We define two slowly varying functions $\Lambda_{n_s}(z)$, and $\psi_k(z)$

$$\Lambda_{n_s}(z) \equiv \int_0^z \left(k_{n_s}(z') - \frac{\omega}{v_{z0}} \right) dz' \quad (22)$$

$$\psi_k(z) \equiv \omega \left(\frac{z}{v_{z0}} - t_k(z) \right). \quad (23)$$

Note that the quantity $\Lambda_{n_s}(z)$ is the same for all particles. It may therefore be computed and stored at initialization time and used

as the simulation proceeds. The final result for the field equation is written as

$$\begin{aligned} & \left(\frac{d}{dz} + \alpha(z) \right) a(z) \\ &= \frac{2\pi i}{I_A} \sum_{k \in T} \sum_m I_k \frac{\mathbf{v}_k(z) \cdot \mathbf{e}_{mn\pm}^*(r_k)}{v_{zk}(z) A_{\text{eff}}^{1/2}(z)} \\ & \cdot \exp[-i(\Lambda_{n_s}(z) - m\theta_k(z) + \psi_k(z))]. \end{aligned} \quad (24)$$

The equations of motion that are integrated together with the field equation are most simply expressed, and numerically integrated, in Cartesian coordinates

$$\frac{d}{dz} \mathbf{p}_k(z) = \frac{q_k}{v_z} \left(\mathbf{E}_k + \frac{1}{c} (\mathbf{v}_k \times \mathbf{B}_k) \right) \quad (25)$$

$$\frac{d}{dz} \psi_k(z) = \omega \left(\frac{1}{v_{z0}} - \frac{1}{v_{zk}} \right). \quad (26)$$

Equations (24)–(26) are a complete description of the steady-state, large-signal model for arbitrary traveling-wave structures, once the space charge fields are included in (25).

B. The Space Charge Field of an Arbitrary Current

To compute the space charge field of an arbitrary beam current flowing in an arbitrary periodic structure, we have generalized the approach used in A-L for a uniform beam traveling in the interior of a helix. The total fields from an arbitrary, spatially periodic current are shown to consist of a pole term, which is identified as the structure field treated in the previous section, and a remainder, which is identified as the space charge field. A similar technique was used by Pierce [27], in one dimension, for the special case of a helix.

The calculation proceeds by computing the response of the structure to a current of the form

$$\mathbf{J}(\mathbf{x}) = \hat{\mathbf{J}}(\mathbf{x}) e^{i(k_z z - \omega t)} + \text{c.c.} \quad (27)$$

where here k_z is *not* the solution of the cold structure dispersion relation, but it is arbitrary. The electric and magnetic fields are similarly represented

$$\mathbf{E}(\mathbf{x}) = \hat{\mathbf{E}}(\mathbf{x}) e^{i(k_z z - \omega t)} + \text{c.c.} \quad (28a)$$

$$\mathbf{B}(\mathbf{x}) = \hat{\mathbf{B}}(\mathbf{x}) e^{i(k_z z - \omega t)} + \text{c.c.} \quad (28b)$$

where $\hat{\mathbf{J}}$, $\hat{\mathbf{E}}$, and $\hat{\mathbf{B}}$ are periodic in z with the structure period. Inside the simulation boundary (Fig. 4), we write the fields as a sum of a particular and a homogeneous solution to Maxwell’s equations

$$\hat{\mathbf{E}} = \hat{\mathbf{E}}_p + \hat{\mathbf{E}}_h \quad (29a)$$

$$\hat{\mathbf{B}} = \hat{\mathbf{B}}_p + \hat{\mathbf{B}}_h \quad (29b)$$

where we will choose the particular solution to satisfy the condition that the tangential components of $\hat{\mathbf{E}}_p = 0$ on the (cylindrical) simulation boundary. This boundary condition is easily implemented in a tridiagonal solver and the particular solution is therefore easily obtained numerically. In order to obtain the homogeneous solution, we proceed as follows.

We first expand the homogeneous solution in a complete set of cold structure modes

$$\hat{\mathbf{E}}_h = \sum_m a_m \hat{\mathbf{e}}_m \quad (30a)$$

$$\hat{\mathbf{B}}_h = \sum_m a_m \hat{\mathbf{b}}_m \quad (30b)$$

where a_m is the amplitude of mode m . Manipulation of Maxwell's equations then gives

$$\frac{4\pi}{c} \int dV \hat{\mathbf{J}} \cdot \hat{\mathbf{e}}_m^* = - \int dS \hat{\mathbf{n}} \cdot [\tilde{\mathbf{E}} \times \hat{\mathbf{b}}_m^* + \hat{\mathbf{e}}_m^* \times \tilde{\mathbf{B}}] \quad (31)$$

where the integral on the left side of (31) is over the volume of the simulation region and the integral on the right side is over its surface. In (31) $\tilde{\mathbf{E}}$ and $\tilde{\mathbf{B}}$ are any solutions to Maxwell's equations; $\hat{\mathbf{n}}$ is the unit outward normal to the surface of the simulation region. If we take $\tilde{\mathbf{E}}$ and $\tilde{\mathbf{B}}$ to be the particular solution, the $\tilde{\mathbf{E}}$ term on the right-hand side of (31) drops out and we have the important relation

$$\frac{4\pi}{c} \int dV \hat{\mathbf{J}} \cdot \hat{\mathbf{e}}_m^* = - \int dS \hat{\mathbf{n}} \cdot [\hat{\mathbf{e}}_m^* \times \hat{\mathbf{B}}_p]. \quad (32)$$

Next, we consider the fields in the region outside the simulation boundary, in the region of the slow-wave circuit. The fields in this region are complicated and must generally be solved for using the CTLSS cold-test solver, but when they are evaluated on the simulation boundary, the tangential components must obey a relation of the form

$$\hat{\mathbf{B}}_t(\mathbf{x}) = \int \frac{dS'}{A} \mathbf{Y}(\mathbf{x}, \mathbf{x}') \cdot (\hat{\mathbf{n}} \times \hat{\mathbf{E}}_t(\mathbf{x}')) \quad (33)$$

where the integral is over the surface of the simulation boundary of area A and \mathbf{Y} is an admittance matrix that may be calculated by the cold-test module. \mathbf{Y} contains information about the structure. Because the tangential fields must be continuous on the simulation boundary, we may use the fields from inside the simulation region, evaluated on the boundary, in (33). Writing the tangential field components as sums of particular and homogeneous parts, as in (29), expanding the homogeneous solutions as in (30), and operating on both sides of (33) with the operator

$$\int dS \hat{\mathbf{n}} \times \hat{\mathbf{e}}_m^* \quad (34)$$

gives an equation for the mode amplitudes

$$D_{mn} a_n = \frac{4\pi}{c} \int dV \hat{\mathbf{J}} \cdot \hat{\mathbf{e}}_m^* \quad (35)$$

where the matrix D is given by

$$D_{mn} \equiv \int dS \hat{\mathbf{n}} \times \hat{\mathbf{e}}_m^* \cdot \left[\mathbf{b}_n - \int \frac{dS'}{A} \mathbf{Y}(S, S') \cdot \hat{\mathbf{n}} \times \hat{\mathbf{e}}_n \right]. \quad (36)$$

Note that D involves only quantities that may be determined by the cold-test module. Once D is found, the total electric field is given by

$$\hat{\mathbf{E}} = \hat{\mathbf{E}}_p + \frac{4\pi}{c} \sum_{n,m} \hat{\mathbf{e}}_n D_{mn}^{-1} \int dV' \hat{\mathbf{e}}_m^*(\mathbf{x}') \cdot \hat{\mathbf{J}}(\mathbf{x}'). \quad (37)$$

This field contains both the structure field and the space charge field. In order to isolate the space charge field (we already treated the structure field in Section III-A, above), we must find a way to subtract out the structure field. To do this, we first note that if we substitute the current (27) in (16) and solve for the structure field amplitude, the resulting expression has a pole as a function of k_z , for $k_z = k_{z0}$ = the cold structure propagation constant. This suggests that if we can isolate the singular part of (37) as a function of k_z , the remaining (i.e., nonsingular) part is the space charge field we are after. Note that the particular solution $\hat{\mathbf{E}}_p$ has no singular part, because from its definition, it must vanish as the beam current tends to zero; this means that $\hat{\mathbf{E}}_p$ cannot be supported by the structure alone.

It follows from (35) that the dispersion relation for the cold structure ($\hat{\mathbf{J}} = 0$) may be written as $\det(D) = 0$. Considered as a function of k_z , therefore, D_{mn} must become singular when $k_z = k_{z0}$. If k_z is close to k_{z0} , this fact may be used to obtain an approximate expression for D^{-1} . To do so, we rewrite (35) as

$$D_{mn}(k_z) a_n = \frac{4\pi}{c} \int dV \hat{\mathbf{J}} \cdot \hat{\mathbf{e}}_m^* \equiv \mathcal{J}_m. \quad (38)$$

To solve (35) for the amplitudes a_n , we expand around the cold structure solution

$$a_n = \mathcal{A} u_n + \delta a_n \quad (39)$$

where u_n is the cold structure eigenfunction and \mathcal{A} is a coefficient to be determined. Substituting in (38) and expanding the matrix D , we obtain to first order in $(k_z - k_{z0})$

$$D_{mn}(k_{z0}) \delta a_n + (k_z - k_{z0}) \frac{\partial D_{mn}}{\partial k_z} (k_{z0}) \mathcal{A} u_n = \mathcal{J}_m \quad (40)$$

where we have used

$$D_{mn}(k_{z0}) u_n = 0. \quad (41)$$

It follows that

$$\mathcal{A} = \frac{u_m^* \mathcal{J}_m}{(k_z - k_{z0}) \left(u_m^* \frac{\partial D_{mn}}{\partial k_z} \Big|_{k_z=k_{z0}} u_n \right)} \quad (42)$$

and

$$D_{mn}^{-1} = \frac{u_m^* u_n}{(k_z - k_{z0}) \left(u_m^* \frac{\partial D_{mn}}{\partial k_z} \Big|_{k_z=k_{z0}} u_n \right)} + Z_{mn}^R(k_{z0}) \quad (43)$$

where $Z_{mn}^R(k_{z0})$ is finite (no pole) as $k_z \rightarrow k_{z0}$. In practice, the space charge field may be obtained by evaluating (37) for (at least) two values of k_z and calculating a best fit to the functional form obtained by substituting (43) into (37). The finite (nonpole) part is then the required space charge field.

IV. DRIVEN-FREQUENCY ELECTROMAGNETIC SOLVER

The CTLSS driven-frequency solver provides a natural means of connecting electromagnetic and large-signal models, where the driving frequency is specified. The solver handles electromagnetic problems in which a driving sinusoidal current source

excites fields in a cavity. The source may be an electron beam, coupling antenna, or waveguide port. In each case, the method of solution for the discretized problem is identical. If the solver is driven with an axial current source at a fixed frequency and axial wavenumber, it can be embedded in an exterior iterative solver to extract the resonant axial wavenumber associated with the specified driven frequency.

A. Solution of the Driven Frequency Problem

The driven-frequency problem implemented by CTLSS solves the discrete form of the linear field equation

$$\left\{ \text{curl} \underline{\underline{\mu}}^{-1} \text{curl} - \omega^2 \underline{\underline{\epsilon}} \right\} \vec{E} = i\omega \vec{J}_s$$

given a frequency ω and source current distribution J_s that includes boundary current sources such as develop in the implementation of waveguide ports. The discrete form of this operator equation is a matrix equation of the standard form

$$\mathbf{A}x = b$$

where \mathbf{A} represents the matrix form of the operator, b is proportional to the known discretized source current vector, and x is the unknown discretized electric field (voltage) vector to be solved. The operator matrix is not stored explicitly, but its action is implemented via a sequence of functions that may be applied to a given field vector, and that satisfy the requirements of linearity and symmetry that the equivalent matrix would possess. Methods of linear algebraic analysis are therefore equally applicable, and matrix methods may be applied.

Numerous methods and algorithms are available for the solution of large, sparse, linear systems, including both direct [28] and iterative [29] solution methods. For our operator, where only the action of the matrix on a field vector is available, iterative algorithms are the most appropriate.

B. CTLSS Matrix Properties

The properties of the matrix operator that develops in the frequency domain formulation are determined by the physical properties of the problem. There are four significant cases, as follows.

- 1) If there are no losses, and if any periodic boundaries have phase advances of 0° or 180° , the matrix that results is purely real and symmetric and, therefore, Hermitian. The eigenvalues are all real and nonnegative, so that the matrix is positive semidefinite.
- 2) If there are no losses, but periodic boundaries exist with arbitrary phase advance angles, elements of the matrix at the periodic boundaries become complex. Provided that the elements are correctly scaled, however, the matrix is still Hermitian and positive semidefinite.
- 3) If there are losses, and if all periodic boundaries have phase advance angles of 0° or 180° , the matrix is complex symmetric. The eigenvalues are no longer real, though for small losses, they lie close to the positive real axis.
- 4) If there are both losses and periodic boundaries having arbitrary phase advance, the resulting matrix has no useful symmetry.

C. QMR—Iterative Matrix Inversion

To solve the system of linear equations, we use the QMR method [5], [30]. This method has some particularly attractive properties for our purpose—it converges almost monotonically even when the matrix is non-Hermitian, yet requires only a small number of workspace vectors. Non-Hermitian matrices frequently cause iterative methods to fail altogether or to diverge periodically from the solution as search vectors become linearly dependent and near-singularities occur in the iterative procedure. The small set of working vectors makes this algorithm attractive in comparison to robust methods, such as GMRES [31], which typically require that a significant size of subspace must be stored.

Advantage may be taken of the matrix symmetry when performing the iterative solution. If the matrix is either Hermitian or symmetric, the computation required at each iteration may be significantly reduced, as pairs of workspace vectors used in the computation become either equal or related by simple complex conjugation of the elements.

When there is no matrix symmetry [(case 4) above], the standard QMR method requires that the transpose of the matrix is available. In CTLSS, the transpose operator may be obtained from the original operator by only a change of sign of the phase advance angles at the Floquet boundaries. Alternatively, it is possible to use a transpose-free variant of the algorithm, TFQMR [32]; however, this algorithm exhibits poorer convergence properties than does the standard QMR algorithm. In each case, convergence of the algorithm is determined based on a relative error defined as the ratio of the Euclidean norms of the residual error and source vectors

$$\eta_k = \frac{\|\mathbf{A}x - b\|_2}{\|b\|_2}$$

where x and b are the field solution and source current vectors, respectively. The target convergence tolerance is set as a user-defined input parameter.

D. Example

Fig. 5 shows a driven-frequency solution of a simple problem geometry that has a wedge of lossy dielectric material ($\epsilon = 43$, $\tan \delta = 0.5$) in the closed end of a rectangular WR10 waveguide, $0.1'' \times 0.05''$ in cross section. A PML boundary region is introduced to attenuate outgoing waves before they reach the end of the solution domain. The driving source is a current sheet that couples selectively to the TE_{10} -mode of the waveguide at a frequency of 68.4 GHz, producing both forward and backward propagating waves inside the waveguide. The forward waves are incident on the wedge and (partially) reflected back to the PML, whereas the backward waves are absorbed directly by the PML region. The problem was discretised on a $24 \times 40 \times 70$ cell uniformly spaced grid, with 201 600 complex unknown field values. Convergence to a residual error $\eta = 10^{-6}$ took just over 2 h on a 400 MHz Pentium II PC. The S_{11} reflection coefficient was calculated to be -17.6 dB, which compares well with a calculation from the HFSS code (Ansoft Corporation) of -16.9 dB. The PML layer was implemented with a thickness of ten cells, and the observed reflection coefficient was -57.6 dB.

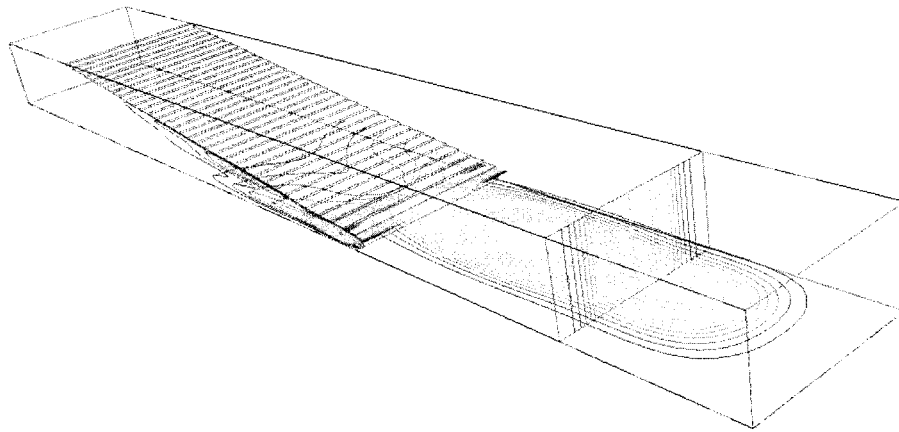


Fig. 5. Contours of electric field energy density inside a rectangular waveguide, terminated by a wedge of lossy dielectric and excited by a TE_{10} planar current source at the position shown. The right-hand end of the solution domain represents a PML region for the outgoing wave boundary condition.

The intensity distribution inside the waveguide and dielectric regions is apparent in the figure. Field concentrations are visible at the apex of the wedge, where strong coupling leads to high absorption in “hotspots” localized at the sides of the waveguide. Standing waves are observed both vertically in the dielectric and axially in the waveguide. The wave is also clearly attenuated inside the PML region well before the end of the solution domain, as suggested by the low observed PML reflection coefficient. The combination of the mode-selective current source and PML layer therefore provides an effective waveguide port boundary condition.

V. RESONANT ELECTROMAGNETIC MODE SOLVER

The resonant eigenmode solver in CTLSS was developed to address the specific requirements encountered in modeling complex electromagnetic structures. The particular issues relating to our discretized operator are the following:

- 1) Problem size—each numerical field vector may hold 10^5 – 10^6 complex elements.
- 2) Complex eigenvalues—lossy materials lead to non-Hermitian operators.
- 3) Zero eigenvalues—the operator has a large null-space that is not of interest to the present computation.
- 4) Conditioning—the matrix may have a large condition number originating from the presence of cells that are small compared with the total computational volume. This typically leads to poor convergence of iterative numerical methods.

Large problem sizes make necessary the use of algorithms with a low workspace overhead, whereas the distribution of the eigenvalues requires that an algorithm is very selective to obtain only the desired solutions. The specific features of the algorithms used and their development are described in this section.

A. Numerical Methods

To obtain the modes of the discretized eigenvalue equation, we choose to use a purely iterative algorithm, so that the matrix need not be expressed or manipulated explicitly.

Iterative methods for the solution of large linear generalized eigenvalue problems fall into a number of categories, including inverse power iteration methods (e.g., inverse power iteration, Rayleigh quotient iteration) and subspace iteration methods (e.g., Arnoldi, Davidson, Jacobi–Davidson, and Lanczos), with variations possible using spectral transformations. The effectiveness of each method depends on the nature of the eigenproblem, particularly the location of the eigenvalues that are to be determined with respect to the overall eigenvalue distribution. With each method, the number of vectors that must be stored during the solution procedure is critical, and it may become a major limitation when problem size exceeds of the order of 10^6 – 10^7 complex unknown field values.

Subspace projection methods represent a general class of methods for the solution of large eigensystems. Such techniques generate and iteratively refine a vector subspace, represented by a small set of basis vectors, such that the converged subspace contains the eigenvectors corresponding to the eigenvalues of interest. The implicitly restarted Arnoldi method [33] is an algorithm of this type that has been applied to many large-scale eigenproblems. It is the basis for the subroutine library ARPACK. We chose to implement an algorithm based on the Jacobi–Davidson procedure [6], without spectral transformations, which offered many attractive features for our purpose and enabled us to tailor the implementation to our specific needs. This algorithm has been applied to large problems in fields of quantum chemistry, acoustics, and magnetohydrodynamics [34].

Although our discrete electromagnetic eigenequation may be analyzed purely as a matrix eigenequation, without reference to its physical derivation, it is useful in practice to take advantage of our knowledge of the structure imposed on the matrix because of its physical origin. This knowledge may be used to accelerate convergence through use of different levels of discretization. Initial solution estimates may be made on coarse grids and used as the starting point of refined estimates. This can significantly improve the algorithm convergence, particularly for fine meshes. In the following sections, the simple matrix eigenproblem is detailed, and then specific adaptations to accelerate our particular problem are outlined.

B. Formulation of the Eigenvalue Problem

The most general type of eigenproblem that we must solve is the complex, nonsymmetric, generalized eigenproblem. To obtain a convergent iterative algorithm for obtaining solutions to this type of matrix problem requires a careful analysis of the properties of the eigenequation [35].

1) *Nonsymmetric Generalized Eigenproblems*: The generalized eigenvalue equation takes the standard form

$$\{\mathbf{A} - \lambda_n \mathbf{B}\}x_n = 0.$$

For the general case when either \mathbf{A} or \mathbf{B} may be non-Hermitian, it is necessary to consider the associated eigenvalue equation

$$y_n^H \{\mathbf{A} - \lambda_n \mathbf{B}\} = 0$$

for the left-hand eigenvectors. The eigenvalues of this system are identical to those of the right-hand system, and corresponding right- and left-hand eigenvectors satisfy a bi-orthogonality relation

$$y_i^H \mathbf{B}x_j = \begin{cases} \zeta_i, & i = j \\ 0, & i \neq j. \end{cases}$$

If degenerate solutions exist, the associated invariant subspaces may be represented by sets of vectors that span that subspace, chosen such that they satisfy the above relation.

To solve non-Hermitian eigenvalue problems, it is useful to consider the right- and left-hand sides of the matrix eigenformulation equally. This has been suggested in connection with the original Davidson method for use with nonnormal matrices [40], whereas a generalized Lanczos solver for nonsymmetric systems was introduced by Cullum *et al.* [36] using a two-sided approach to represent the left and right eigenvector solutions.

2) *Subspace Projection Methods*: The Jacobi–Davidson method makes use of subspace projection to obtain estimates of a few eigenvalues of a large matrix eigenproblem. Here, we summarize this procedure, taking into account the two-sided nature of the nonsymmetric eigenproblem.

Any small, p -dimensional subspace of the full solution space may be represented by a set of p basis vectors in that space. Each vector corresponds to a discretized electric field and may be stored numerically as a column vector of coefficients. A subspace may be represented by a matrix composed of p such columns, so that right and left subspaces, \mathbf{V} and \mathbf{W} , respectively, may be written as

$$\begin{aligned} \mathbf{V} &= \{v_1, v_2, \dots, v_p\} \\ \mathbf{W} &= \{w_1, w_2, \dots, w_p\}. \end{aligned}$$

Using a Ritz–Galerkin procedure, we may obtain an estimate of the eigensolution projected on these subspaces. Assuming right-hand eigenvector estimates x_m are constrained to lie within V , and left-hand eigenvector estimates y_m in W , we may write

$$x_m = \mathbf{V}s_m, \quad y_m = \mathbf{W}t_m$$

where vectors s_m and t_m of length p are to be determined. We can express the right and left residual error vectors for the eigenequation

$$r_m = (\mathbf{A} - \theta_m \mathbf{B})x_m, \quad q_m^H = y_m^H (\mathbf{A} - \theta_m \mathbf{B})$$

and require that the projection of this error onto the other subspace is zero

$$\begin{aligned} \mathbf{W}^H r_m &= \mathbf{W}^H (\mathbf{A} - \theta_m \mathbf{B}) \mathbf{V} s_m = 0 \\ q_m^H \mathbf{V} &= t_m^H \mathbf{W}^H (\mathbf{A} - \theta_m \mathbf{B}) \mathbf{V} = 0. \end{aligned}$$

This is equivalent to the projected pair of right and left eigenequations

$$\begin{aligned} (\mathbf{P}_A - \theta_m \mathbf{P}_B) s_m &= 0 \\ t_m^H (\mathbf{P}_A - \theta_m \mathbf{P}_B) &= 0 \end{aligned}$$

having right and left solution vectors s_m and t_m , respectively, where the small projected matrix operators are defined as

$$\begin{aligned} \mathbf{P}_A &= \mathbf{W}^H \mathbf{A} \mathbf{V} \\ \mathbf{P}_B &= \mathbf{W}^H \mathbf{B} \mathbf{V}. \end{aligned}$$

By obtaining solution eigenvectors to the projected eigenproblem using a solver for dense matrices, we may obtain their representations in the full solution space x_m and y_m corresponding to each value θ_m , termed the right and left Ritz vectors and Ritz value, respectively. The dense, generalized eigensolver routine used to solve the projected eigenproblem was taken from the LAPACK library [37].

The subspace projection step forms part of the nonsymmetric Jacobi–Davidson algorithm [38]. The other main component is the modification of the subspaces V and W to ensure their convergence to subspaces that contain the solution eigenvectors of interest. The Hermitian and complex-symmetric cases may be recovered straightforwardly from the nonsymmetric case by fixing $\mathbf{W} = \mathbf{V}$ or $\mathbf{W} = \mathbf{V}^*$, respectively, in the following description.

C. Jacobi–Davidson Method

The Jacobi–Davidson algorithm is depicted in Fig. 6. As described by Sleijpen *et al.* [6], a single subspace is used to span the subspace of right eigenvectors, and either the same subspace or one derived from it is used for the left-subspace projection. A theory for the generalized eigenproblem using a single subspace is outlined by Booten *et al.* [34]. Here, we describe the algorithm for the general, nonsymmetric case using two subspaces and a combined subspace refinement procedure.

Beginning with an initial seed subspace, or pair of subspaces for the nonsymmetric case, iterations of the outer loop modify the subspaces by first estimating eigensolutions by subspace projection, and then selectively applying an orthogonal correction procedure to correct or extend the subspaces. The correction step is related to that of the block Galerkin inverse iteration (BGII) method [39], but the correction vectors are determined only approximately, and they are used to extend the subspaces, as in the Davidson method [8], [40], to promote an improved solution estimate at the next iteration.

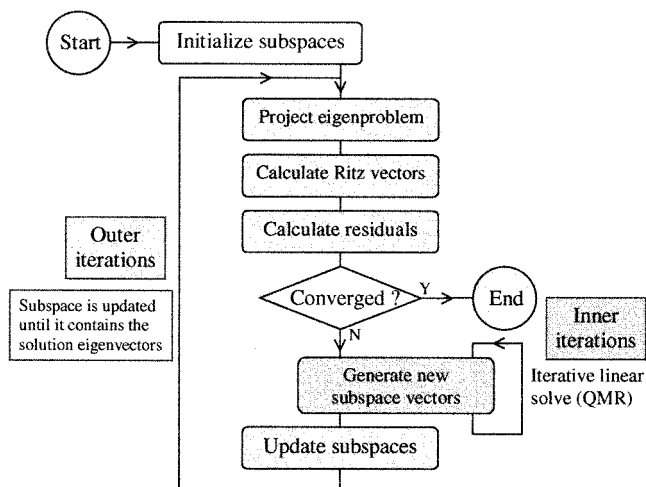


Fig. 6. Flow diagram of the Jacobi–Davidson algorithm.

To limit the maximum subspace size that must be stored, this procedure is typically restarted after some fixed number of iterations, at which time the subspace is contracted to include only a few of the solution estimates that lie closest to the desired eigensolutions. The process of subspace expansion then recommences.

In place of this approach, we describe in Section V-D a subspace management strategy that minimizes the use of computational resources. There is no explicit restart step, as the subspace size is carefully managed at each iteration. A similar procedure has been suggested for the Arnoldi method [33]. In addition, for very poorly converged eigenvalues, we use approximate inverse iteration in place of orthogonal correction to enhance the initial convergence to the desired frequency range.

The following sections detail the steps of the algorithm.

1) *Subspace Convergence*: At the beginning of each outer iteration, the Ritz vectors and residual error vectors are determined for the current subspaces by subspace projection. The Ritz vectors represent the best approximation within the subspaces to the eigenvector solutions, whereas the residuals contain information in the full solution space, orthogonal to the current subspaces.

To determine convergence of the Ritz vectors to eigenvectors, we evaluate a measure of the error based on the Euclidean norm of the residual vector. We define the normalized convergence parameter for each Ritz vector

$$\rho_m = \frac{\|(\mathbf{A} - \theta_m \mathbf{B})x_m\|_2}{\|\mathbf{A}x_m\|_2}$$

and compare this value at each iteration of the outer loop with a specified tolerance, typically, $\approx 10^{-2}$ – 10^{-3} , performing correction steps only on remaining unconverged vectors, so that all solutions are finally converged to the same specified level. The eigenvalue converges at a faster rate, typically, $O(\rho_m^2)$.

To generate new subspace vectors, the Jacobi–Davidson method searches for a correction vector orthogonal to the current Ritz vector that reduces the norm of the residual. It is not necessary to obtain the minimum value, as in any case the residual is calculated using only the approximate Ritz value.

A moderate improvement is sufficient, and it may be obtained using a number of iterations of an iterative procedure. As the Ritz value estimate improves, it becomes increasingly effective to iterate closer to the optimal correction. In the following sections, we outline the orthogonal correction step for the nonsymmetric case.

2) *Orthogonal Projection*: The right and left eigenvectors of the solution to the projected eigensystem possess the same biorthogonality relation as do those of the full eigensystem. For the simplest case in which eigenvalues are distinct, pairs of non-degenerate eigensolutions satisfy

$$t_i^H \mathbf{P}_B s_j = 0, \quad i \neq j.$$

From this relation, a similar biorthogonality relation is retained for the Ritz vectors

$$y_i^H \mathbf{B} x_j = 0, \quad i \neq j$$

and therefore pairs of distinct right and left Ritz-vectors are biorthogonal with respect to \mathbf{B} .

To improve each eigenvector estimate, we search for a correction vector orthogonal to the current Ritz vector that brings our estimate closer to the solution vector. To implement this step in the following section, we will require operators that perform this projection. We define orthogonal projection operators

$$\mathbf{P}_k^\perp = \mathbf{I} - \frac{x_k y_k^H \mathbf{B}}{y_k^H \mathbf{B} x_k}, \quad \mathbf{Q}_k^\perp = \mathbf{I} - \frac{\mathbf{B} x_k y_k^H}{y_k^H \mathbf{B} x_k}$$

that project orthogonally to the given Ritz vectors to the right and left, respectively.

3) *Jacobi Orthogonal Component Correction*: The Jacobi–Davidson algorithm for a single subspace uses each right-hand residual vector to generate a new vector that is orthogonal to the corresponding Ritz vector by obtaining an approximate solution to a projected linear system of equations. Typically, this is performed using a few iterations of an iterative linear solver. Because we are using separate left and right subspaces, we generate for each Ritz value of interest a pair of correction vectors z_k and u_k that satisfy a biorthogonality relationship to the current right and left Ritz vectors. We solve, approximately, for correction vectors z_k and u_k in the two independent systems of linear equations

$$\begin{aligned} \mathbf{Q}_k^\perp (\mathbf{A} - \theta_k \mathbf{B}) \mathbf{P}_k^\perp z_k &= -r \\ u_k^H \mathbf{Q}_k^\perp (\mathbf{A} - \theta_k \mathbf{B}) \mathbf{P}_k^\perp &= -q_k^H. \end{aligned}$$

In principle, the search could be made completely orthogonal to the current subspace, over which the residuals are already optimal following the Ritz–Galerkin procedure. This would introduce products of projection operators, computed using a modified Gram–Schmidt procedure. The single projection step was found to be sufficient in practice, and further projection only added unnecessary computation.

Because the above equations contain the same product of operators, they may be solved in a single procedure using an iterative algorithm such as QMR or the biconjugate gradient method. In our implementation, we used the QMR method, which even for nonsymmetric matrices reduces the residual error almost

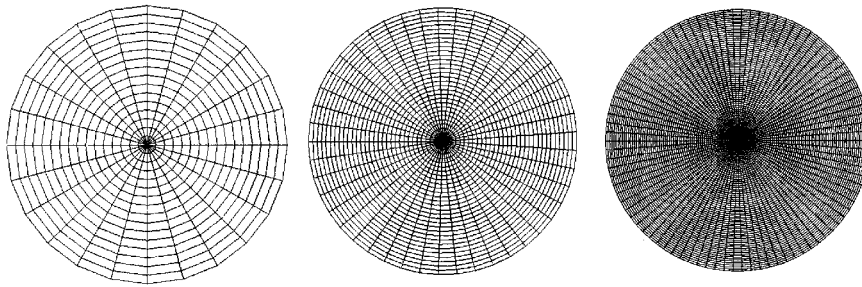


Fig. 7. Three resolutions of grid representation for a helix TWT structure.

monotonically with only a small set of workspace vectors. Using q_k to generate the left-hand correction and r_k for the right-hand correction, we may use QMR directly to solve both sets of equations simultaneously.

The convergence of the iterative QMR algorithm is controlled based on a relative convergence parameter, defined for the i th (inner) iteration,

$$\eta_k^{(i)} = \frac{\|Q_k^\perp(\mathbf{A} - \theta_k \mathbf{B})P_k^\perp z_k^{(i)} + r_k\|_2}{\|r_k\|_2}$$

QMR terminates when either the error criterion is reached, or if numerical breakdown occurs in the underlying Lanczos process. The occurrence of premature termination caused by numerical breakdown is not catastrophic here, because the resulting approximate solution is adequate for continuation of the Jacobi–Davidson method, and convergence will be resumed at the next outer iteration. Therefore, to avoid the additional storage necessary, no look-ahead procedure [41] is performed.

Ideally, if the update equations are solved exactly, the Jacobi–Davidson method can achieve cubic convergence for symmetric matrices (quadratic convergence for the nonsymmetric case), requiring very few outer iterations. However, a balance exists between solving the equations to full precision a minimal number of times and solving approximately over a greater number of iterations. Typically, the overall cost was found to be reduced using approximate solutions, though the eigenvalue convergence deviates from being cubic (quadratic). In principle, the rate of convergence of the Jacobi–Davidson algorithm may be greatly accelerated if a good preconditioner is available to improve conditioning of the linear solution step [42]. Simple preconditioning is applied by symmetrically scaling the operators by the diagonal matrix $D_C^{-1/2}$ and solution field vectors by $D_C^{1/2}$, which leads, for orthogonal coordinate systems, to a standard type of eigenproblem. If a more complex preconditioner were available, the preconditioned variant of the QMR algorithm could be applied.

D. Subspace Update Strategy

To begin, a set of subspace vectors is initialized either randomly, effectively populating all component eigenmodes with random amplitudes, or from a seed subspace if an approximate field solution is available. Each pass of the algorithm acts to selectively filter out unwanted frequencies from this initial field. Because all subsequent vectors are derived systematically from this initial set by successive application of the operators, the

multiplicity of degenerate solutions that can be determined is limited by the number of linearly independent initial vectors that are defined. A single vector is sufficient to seed the solution in the absence of degeneracy.

At each step, following subspace projection, we first filter the subspace on the basis of the determined Ritz values by specifying a desired range of eigenvalues (or circle in the complex plane) or a limit on the number of solutions to be determined. Ritz vectors having Ritz values outside the target region are selected for removal from the subspace, subject to two restrictions: 1) sufficient vectors are kept to maintain the initial level of linear independence for degenerate solutions, and 2) an upper limit to the number kept is set at the number of solutions requested. In each case, values closest to the center frequency are retained preferentially, and the subspace vectors are ordered accordingly.

For each remaining Ritz vector, the error term ρ_k is calculated and compared with the specified convergence tolerance. Those that have not yet reached the specified convergence level are next updated in turn, whereas converged solutions are simply kept in the subspace. For Ritz values inside the target range, approximate corrections are obtained using orthogonal projection with QMR, as for the original Jacobi–Davidson algorithm, using the Ritz value as the shift in the operator. The default target for convergence is $\eta_k \approx 0.1$, a value selected to minimize the overall convergence time. The resulting correction vector is used to extend the subspace, though the number of extensions in any iteration is limited to typically one or two vectors to minimize memory usage. Remaining corrections, and in particular corrections for well-converged solutions having residual errors $\rho_k < 10^{-4}$, are added to the corresponding Ritz vectors directly, as in the BGII method [40]. It is observed that for moderately well converged vectors, the error ρ_k in the next iteration is smaller by a factor $\approx \eta_k$.

Ritz values outside the target range are updated using approximate inverse iteration, with the center frequency of the target range as the shift in the operator. The approximate solution replaces the Ritz vector in the subspace. This acts to enhance the components of the desired eigenvectors before reasonable eigenvalue approximations are available. A target convergence $\eta_k \approx 10^{-2}$ – 10^{-3} is found to be effective.

The above procedure maximizes the retention of information in a subspace that is only a few vectors larger than is the number of solutions sought. The update steps, the most computationally intensive phase of the solution, provide an inherent coarse-grained parallelism. In principle, each update may be performed independently.

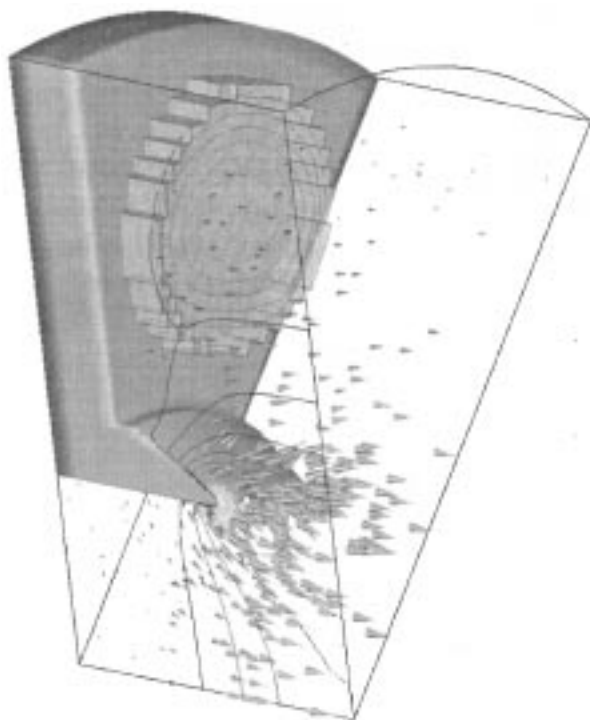


Fig. 8. View of klystron simulation region (1/16th of cavity), showing electric field vectors (arrows) and contours of electric energy density, spaced at 2% intervals, visible in the ceramic load and gap regions. Mode frequency 3.097 GHz, $Q = 40.7$.

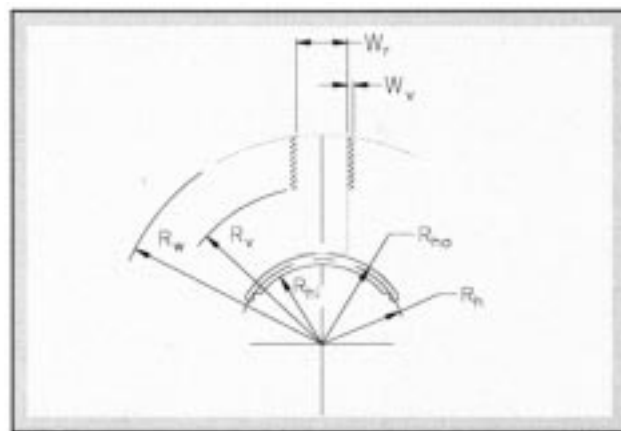


Fig. 9. Vaned TWT circuit. Metallic vanes strongly couple to the operating mode. Parameters are selected to achieve a flat dispersion curve.

TABLE I
CALCULATED EIGENFREQUENCY VERSUS. PHASE ADVANCE PER CELL (IN DEGREES) FOR A COUPLED-CAVITY TWT CIRCUIT

Phase	Mode 1	Mode 2	Mode 3	Mode 4
0	89.871	121.993	121.576	121.576
15	89.955	121.538	121.583	121.583
30	90.207	120.332	121.603	121.603
45	90.623	118.665	121.635	121.635
60	91.202	116.756	121.677	121.677
75	91.940	114.733	121.725	121.725
90	92.832	112.666	121.778	121.778
105	93.878	110.600	121.831	121.831
120	95.051	108.560	121.880	121.880
135	96.365	106.569	121.922	121.922
150	97.805	104.641	121.955	121.955
165	99.361	102.790	121.976	121.976
180	101.026	101.026	121.983	121.983

E. Multilevel Solution

When the problem size increases, the condition number of the matrix becomes very large, and iterative methods converge very slowly. Multigrid solutions are applicable to this type of problem and take advantage of the known structure of the physical problem. Integration of full multigrid (FMG) with the CTLSS eigensolver has not yet been performed; however, a hierarchy of grids is used in the solution of the eigenproblem.

Once the problem has been defined on the finest level of grid, an averaging procedure is applied to the capacitance and inductance terms to generate a related problem having half the number of cells in each dimension. The number of field values is thereby reduced by a factor of eight for a 3-D problem, and the solution at the coarser level is much faster than is the full solution. A so-

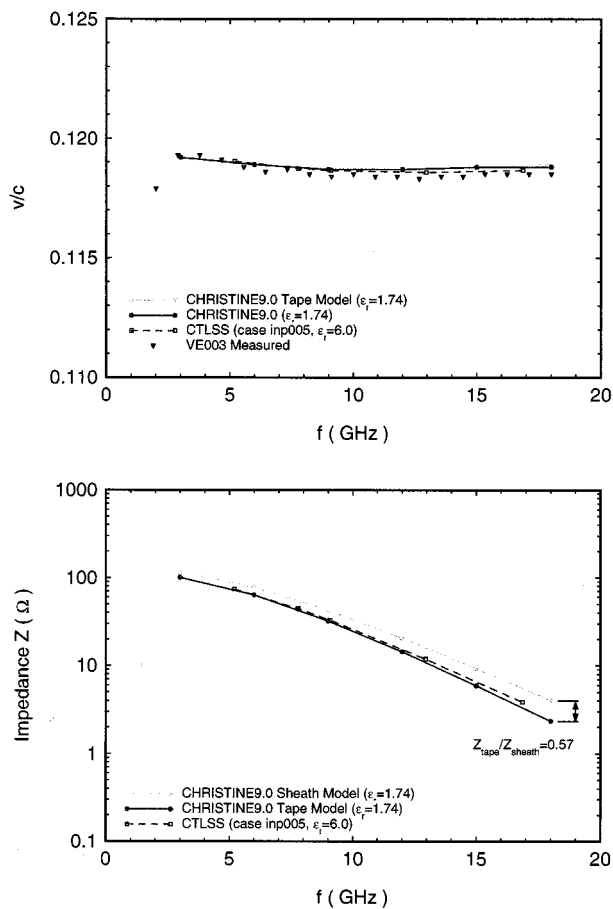


Fig. 10. Mode dispersion and coupling impedance for a vaned helix-TWT circuit (data courtesy of Northrop Grumman).

lution subspace obtained at this level is interpolated to the finer grid as an initial subspace for the larger problem. By this procedure, much of the effort required to approach the desired solution at the finest grid is circumvented. At the finest level, only a few refinement steps are necessary. This method was found to be very effective, and typically, two levels of approximation are applied to further accelerate the process.

Fig. 7 shows an example of three successive levels of solution for helix TWT geometry at high resolution. During the CTLSS

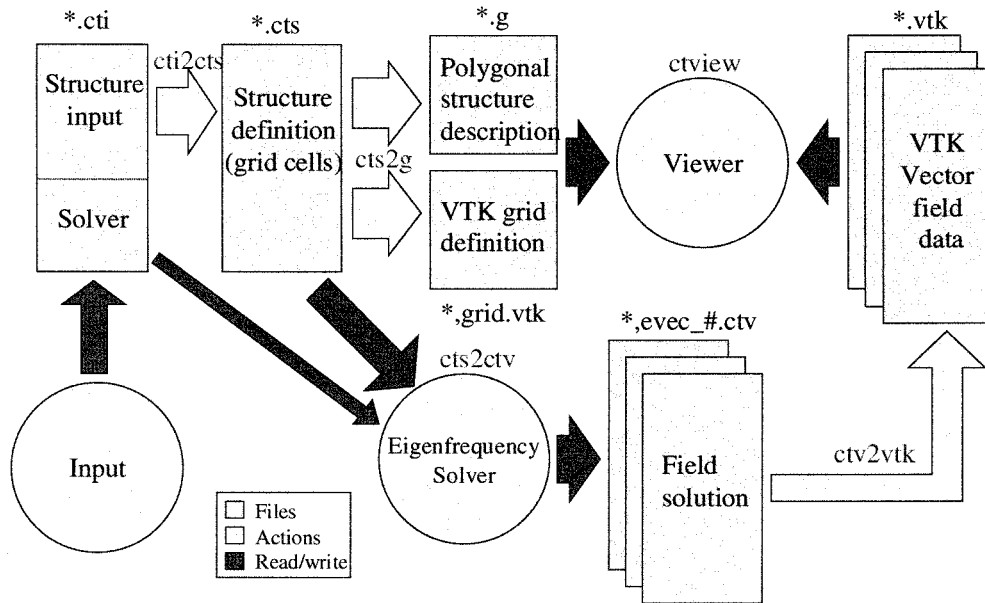


Fig. 11. CTLSS modules.

validation phase of the program, the multigridding function was evaluated and determined to provide significant reduction in execution times over systems that did not use the multigridding function. For a case that employed the optimum gridding for helix TWT geometry, providing the best balance between solution accuracy and execution times, two levels of multigridding were used on a $32 \times 36 \times 32$ grid, and resulted in a reduction in run times of approximately $2.5\times$. In this case, nearly identical eigenfrequencies were computed with and without the multigridding function, whereas execution times were reduced from 4.9 h to 2.0 h. Larger simulations, such as the one depicted in Fig. 7, would benefit even more from use of this function.

F. Examples

To illustrate the present capabilities of the CTLSS code, we present a number of examples taken from real devices.

1) *Example 1: Klystron Cavity:* A klystron cavity, depicted in Fig. 1, was modeled using a cylindrical coordinate mesh, with nonuniform spacing of cells. The cavity consists of a cylindrical pill-box, with coaxial, cutoff cylindrical waveguides protruding into the volume and having the noses radiused and separated by a small gap. Eight absorbing ceramic buttons surround each waveguide on the flat end-walls of the pill-box to control the cavity Q .

Using a combination of symmetry and metal wall boundary conditions, solving only $1/16$ th of the cavity was sufficient to determine the lowest, TM_{011} -mode. This sector was discretized using a $88 \times 32 \times 44$ cell mesh, having 371 712 complex unknown field values. Convergence of the eigenmode solution to a residual error $\rho_k = 10^{-2}$ took 6 h on a 600-MHz Pentium II PC. The eigenfrequency of 3.097 GHz and Q of 40.7 agree well with experimentally determined values, 3.140 GHz, $Q \approx 44$, given the estimated uncertainty in the ceramic dielectric constant of 5%. The long run-time for this example may be attributed to the large dielectric constant, $\epsilon' = 78.25$, and high

loss, $\tan \delta = 0.179$, of the ceramic load used in the simulation that leads to poor conditioning of the problem.

The TM_{011} -mode of the cavity is shown in Fig. 8. The electric field is concentrated across the gap region, whereas a significant energy density inside the ceramic buttons causes strong absorption, leading to the low observed Q .

2) *Example 2: Coupled Cavity TWT:* A section of a coupled cavity TWT circuit is also shown in Fig. 1. The structure of this device is periodic, with the unit cell shown. Approximating the finite circuit structure by an infinite structure, its dispersion characteristics may be obtained by applying a Floquet boundary condition parameterized by the phase advance angle [43]. In this case, the full unit-cell structure was modeled to obtain all types of mode symmetry. It would be possible to reduce the computation time significantly by applying either electric-wall or magnetic-wall boundary conditions at the two planes of reflection symmetry that exist.

The simulation was performed on a $64 \times 64 \times 40$ cell mesh (491 520 complex unknowns). Convergence of all four eigenmodes to a residual error $\rho_k = 10^{-2}$ took 40 min per phase angle, on a 400-MHz Pentium II PC.

Table I shows the frequency dispersion of each of the first four modes, determined by CTLSS. Modes 3 and 4 are degenerate.

3) *Example 3: Helix TWT Circuit, with Vanes:* To control the dispersion properties of a helix traveling wave interaction circuit, metallic vanes are introduced as coatings on the dielectric supports as shown in Fig. 9. A careful choice of dimensions allows an almost constant phase velocity to be achieved over a very wide frequency band.

Using CTLSS, the dispersion characteristics were obtained using a mesh with $35 \times 67 \times 17$ cells, in a cylindrical geometry. The structure is doubly periodic, in the azimuthal and axial coordinates. Using a Floquet boundary condition axially, the dispersion was calculated for the vanned circuit, as shown in Fig. 10. The effect of the vanes is in flattening the wave phase velocity, and the flatness predicted by CTLSS agrees very well with the

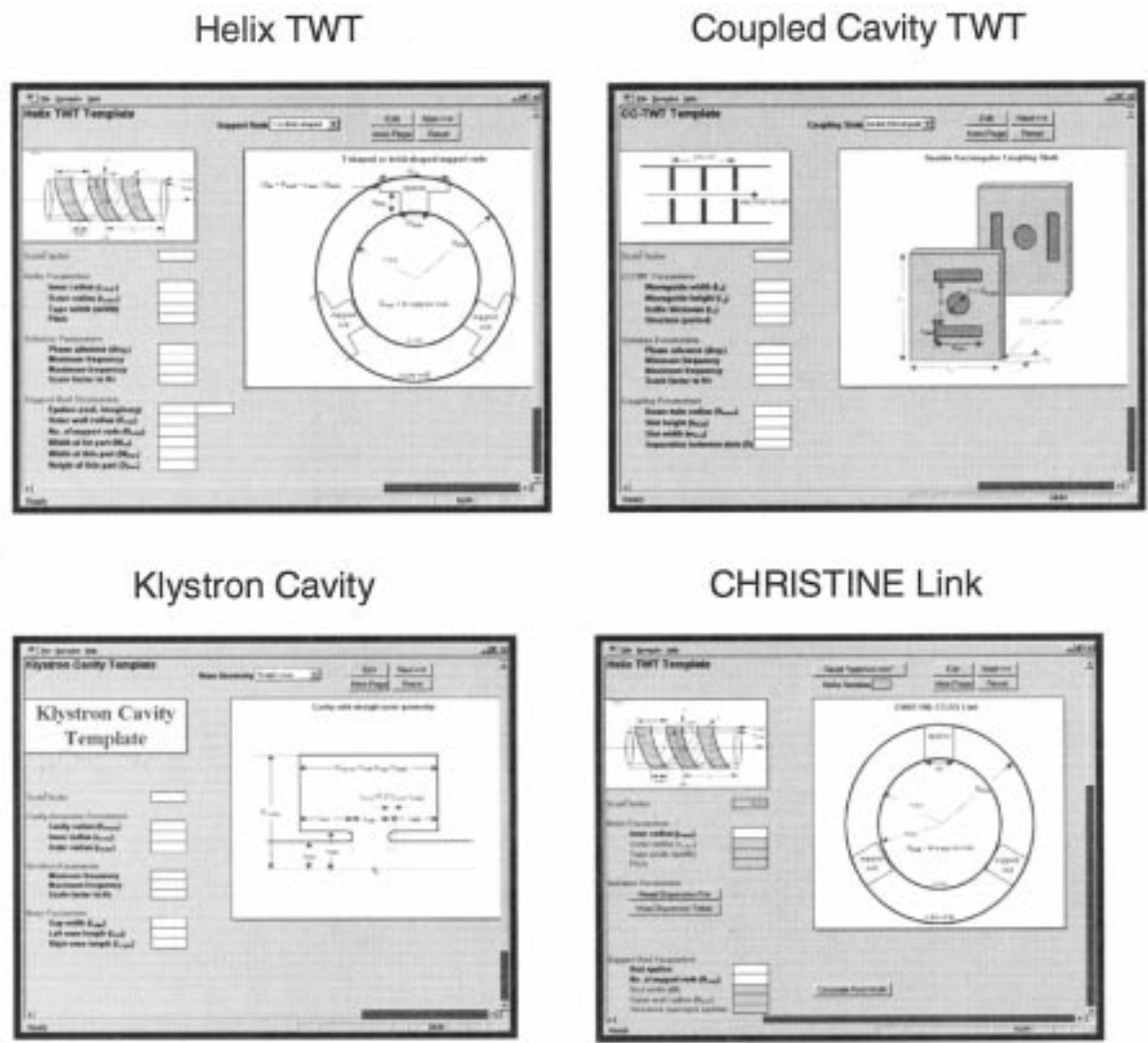


Fig. 12. CTLSS templates.

experimental data. The CHRISTINE dispersion curves are calculated from the semianalytic sheath and tape helix models, using an arbitrary effective permittivity parameter chosen to fit to an average of experimentally determined values.

Comparisons between CTLSS and measured phase velocity data were obtained for an unvaned circuit and three separate vaned circuits. The grid size used in Fig. 10 was $35 \times 67 \times 17$, though a case with $35 \times 91 \times 17$ also showed good convergence. The azimuthal cell size was reduced significantly at the sides of the rod to properly resolve the thin vanes. The agreement for phase velocity with experimental data is good (note the compressed range on the y -axis). The agreement with the CHRISTINE codes (for the sheath helix and, more accurate, tape helix models) is also very good, provided that the “effective” dielectric constant in CHRISTINE is adjusted as indicated.

Fig. 10 also shows the coupling impedance obtained for this structure from the calculated field, which describes the integrated coupling to the RF electric field experienced by electrons passing along the axis. The effect of the vanes is to reduce the coupling impedance slightly, but to permit interaction across a very wide bandwidth. The calculated impedance across the fre-

quency range with a tape helix shows a large impedance drop at the high end of the band, confirmed by the CTLSS data. The cause of this impedance drop is still not resolved, and measurements on cold-test circuits are in progress to try to gain a better understanding.

VI. CTLSS CODE

The CTLSS code has been highly modularized so that its multiple functions can share common utilities between modules. CTLSS itself functions as a module in the modeling and simulation tool suite, which includes MICHELLE and CHRISTINE, and shares postprocessing, visualization, and gridding tools with those programs. Future development is aimed at tightening the integration of these codes.

The current release version of CTLSS consists of the electromagnetic eigenvalue solver on a single-block orthogonal structured mesh, a graphical user interface (GUI), a postprocessor to compute phase velocity and impedance for specified modes, a visualization tool and interface for 3-D structure and vector field plots, and a data link to CHRISTINE. The design methodology

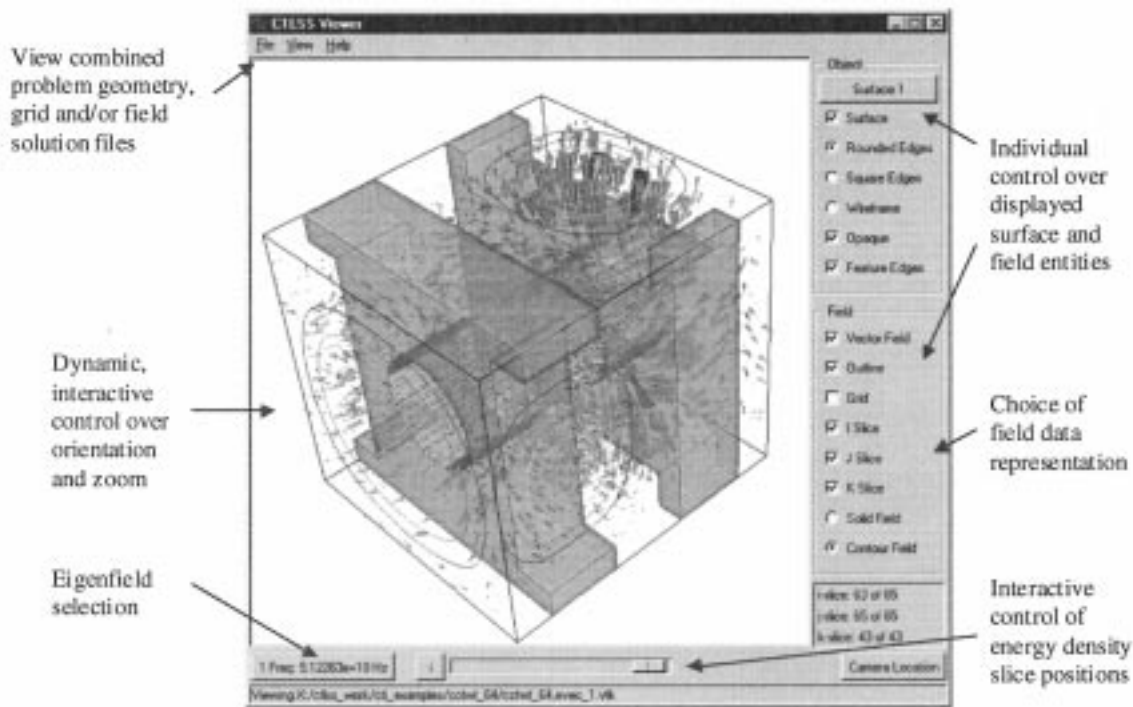


Fig. 13. CTLSS solution viewer.

for vacuum electronic devices (currently helix-TWT configurations) integrated into CTLSS is the following.

- 1) CHRISTINE is employed as a stand-alone code to compute an optimum helix-TWT configuration (which may consist of several helix sections with different parameters.)
- 2) The output of CHRISTINE for a specified helix section is read into the GUI, where the user specifies additional parameters that are not needed by CHRISTINE, but are required to run CTLSS. The GUI then calculates all remaining parameters, such as the dimensions of the support rods, and generates a basic structure definition so that a CTLSS *.cti input file can be created. The GUI also writes a new CHRISTINE input file that can be executed after the CTLSS runs in step 3) are completed.
- 3) CTLSS is used to compute the dispersion and impedance data for the CHRISTINE configuration, including 3-D effects, such as actual support rods and finite thickness tape helix geometry, in place of the idealized smeared dielectric, and the sheath helix or thin tape helix models in CHRISTINE.
- 4) A new CHRISTINE run, using the computed cold-test results from CTLSS, can assess the change in performance of the helix TWT because of the effects included by CTLSS.

This cycle may be repeated to converge upon an optimal, realistic design.

A. Code Structure

The code is a hybrid of Fortran and C++ modules, with the parts of the code specific to data input and the electromagnetic operators (including setup routines, curl-operator routines, and

boundary conditions) largely written in Fortran for efficiency, whereas the controllers for the Jacobi–Davidson and QMR routines and overall data structures are written in C++. Classes are defined to encapsulate the problem description, coordinate systems, matrix operators, fields, and subspaces, with their associated operations. The underlying linear algebra libraries used for vector and dense matrix operations, BLAS and LAPACK, are also either native Fortran routines or available optimized for a particular platform.

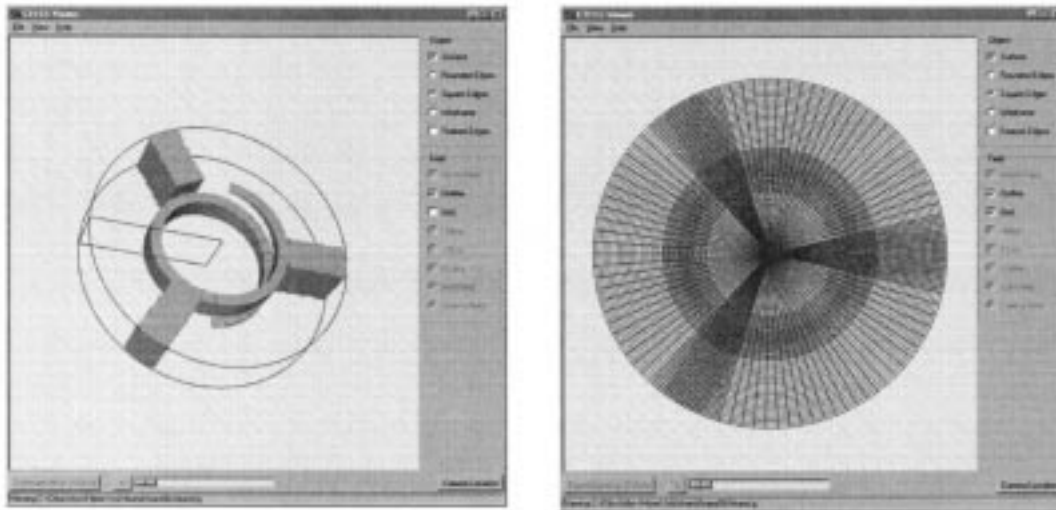
B. Modules

The modular structure of CTLSS is illustrated in Fig. 11. The user constructs a text input file (*.cti), either manually or with the help of a GUI, and runs a setup program, *cti2cts*, to create a structure file (*.cts). The eigenvalue solver, *cts2ctv*, reads both the *.cti and *.cts files to produce a file of solution field vectors (*.ctv). Two postprocessors, *cts2g* and *ctv2vtk*, convert the structure and field output files into formats that can be used by the visualization toolkit (VTK) to render 3-D images of the fields and structures. Finally, a third postprocessor (not shown), *ctv2imp*, reads the field output file and processes impedance and phase velocity for a specified solution vector (mode.)

C. GUI

A GUI has been created for CTLSS in Excel Visual Basic. It is a general interface that governs structure input and grid setup, as well as specification of all control parameters required by the code, and provides the user with simple definitions of input quantities. The interface also includes a series of templates designed to automate the definition of commonly used device configurations, such as the helix TWT, the coupled-cavity TWT, and the klystron. The output of the GUI is the *.cti input file

Cylindrical Geometry



Cartesian Geometry

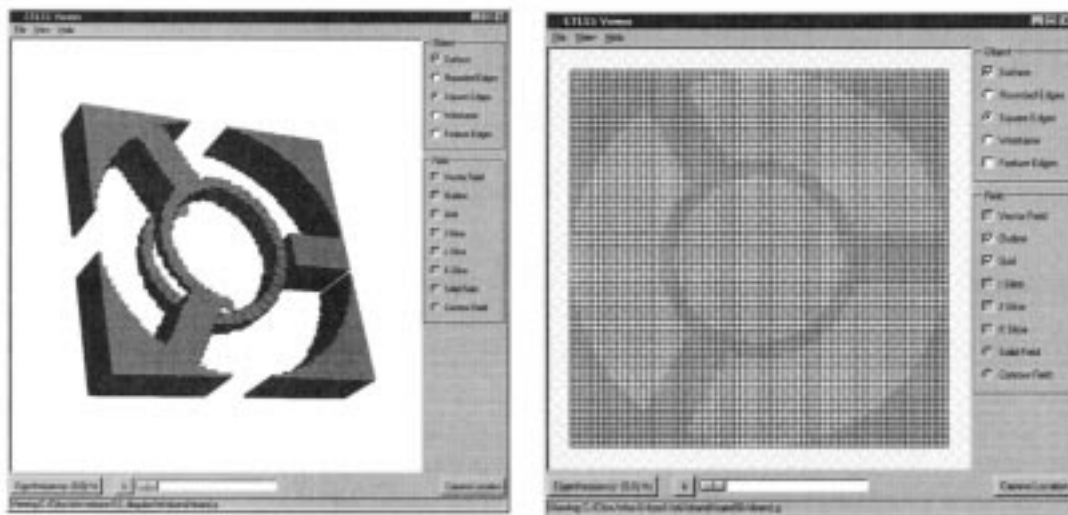


Fig. 14. Helix TWT represented in cylindrical and Cartesian coordinates.

required to run CTLSS. The GUI can also read in the *.cti file for editing, and it can invoke a setup run with visualization.

The major sections of the CTLSS GUI “Setup” and “Eigensolver” controls. The Setup section includes General Setup, Boundary Conditions, Structures, and Gridding, which are required to run the setup module. The Eigensolver section includes General Controls and Eigensolver sheets, which set up the eigensolver module.

The CTLSS templates, illustrated in Fig. 12, allow the user to rapidly set up specialized configurations. The helix TWT template, for example, includes several options for support rod shapes (with user-specified dimensions). The coupled-cavity TWT includes several options for the number and shape of the coupling slots between the cavities. The klystron template has

several options for the shape of the cavity nose structure. These templates automatically populate the general CTLSS GUI, so that the user can modify the automatic setup, as needed, to execute a specific simulation.

An additional template automatically sets up the link between CTLSS and CHRISTINE for designing helix TWT circuits, using the methodology described above.

D. Visualization

CTLSS uses the VTK to create 3-D graphical renderings of the discretized structures and field solutions. The VTK system is programmed in Tcl/Tk, to produce customized plots and to provide a GUI specifically for viewing CTLSS output (see Fig. 13.)

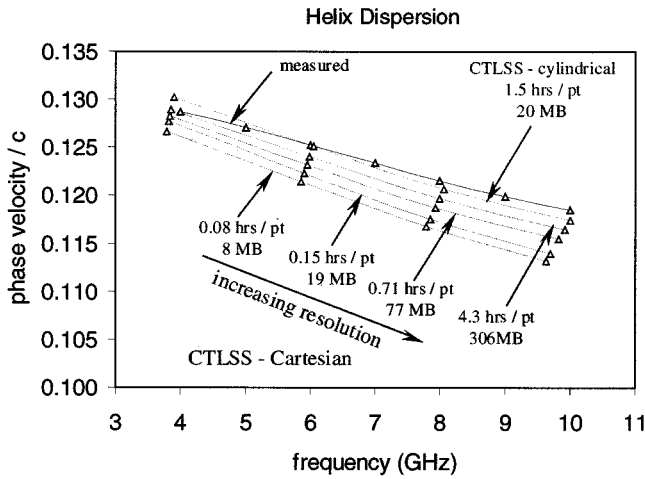


Fig. 15. CTLSS results for a helix TWT. Run times and memory requirements for several Cartesian and cylindrical setups are compared with measured data from a Northrop Grumman Corporation X-Band TWT.

The viewer for the current CTLSS code is being absorbed into a postprocessor and viewer developed for all of the modeling and simulation tools.

E. Gridding

The current CTLSS release version supports both Cartesian and cylindrical coordinate systems. The advantage of having both options is that one or the other system will be more conformal with the structure and, therefore, will require fewer cells and less run time.

Fig. 14 shows a comparison of Cartesian and cylindrical gridding for a helix TWT. In this case, the cylindrical coordinate system is better because it is important to resolve the tape helix thickness, which need only be resolved in the radial direction in cylindrical geometry, but it requires fine gridding in both x and y in Cartesian geometry. The eigenvalue solver is also remarkably tolerant of large changes in cell size from cell to cell. Hence, it is permissible to arrange the azimuthal grid so that it becomes much denser on the support rods than it is between the rods, thereby gaining better resolution and discretization of the rods for a given total number of cells.

A comparison of the run time for a helix TWT in optimized cylindrical and Cartesian geometry was carried out at Northrop Grumman Corporation [44], with the results shown in Fig. 15. Computations were performed on a 450-MHz Pentium II PC, having 384-Mb available RAM. The cylindrical mesh was $34 \times 48 \times 16$ cells, whereas the Cartesian meshes were $32 \times 32 \times 16$, $40 \times 40 \times 16$, $80 \times 80 \times 16$, and $160 \times 60 \times 16$ cells.

Fig. 15 shows that the cylindrical setup, requiring only 20 MB of memory and 1.5 h per data point, outperforms setups in Cartesian geometry using up to 306 MB and 4.3 h per data point.

F. Postprocessing

The CTLSS postprocessor computes the axial impedance and the phase velocity for a specified eigenfield solution, as well as field energy density. The driven-frequency module includes the calculation of S parameters for specified ports.

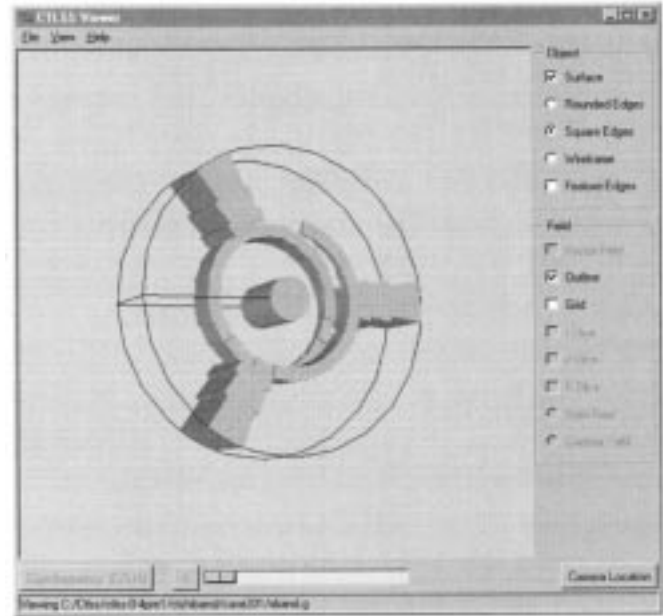


Fig. 16. Perturbation method for experimentally determining axial impedance.

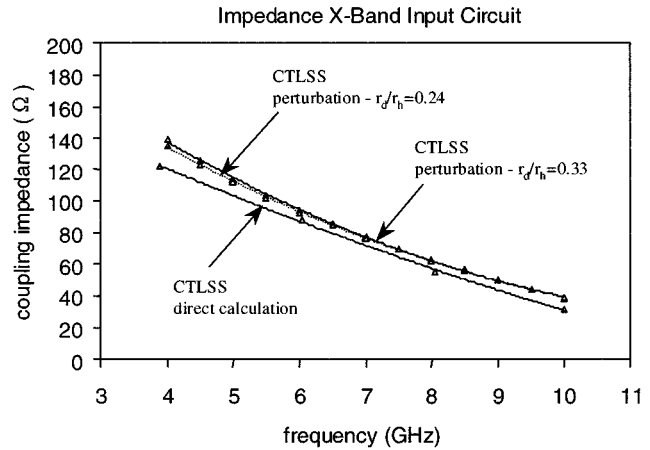


Fig. 17. Coupling impedance as determined by direct calculation using 3-D CTLSS fields, CTLSS simulation of a perturbation experiment with $r_d/r_h = 0.24$, and CTLSS simulation of a perturbation experiment with $r_d/r_h = 0.33$.

The ability of electromagnetic simulation codes to accurately compute the axial impedance for TWT's has been an issue for several years. Recently, that issue has been resolved in favor of the simulation codes [44], [45]. The axial impedance is computed from first principles as

$$Z_0 = \frac{|E_z(r=0)|^2}{2\beta^2 P}$$

where E_z is the lowest order Fourier component of the electric field on axis, $\beta = \omega/v_p$ is the wavenumber, v_p is the phase velocity, and P is the time-averaged RF power flow

$$P = \frac{1}{2} \text{Re}(\vec{E} \times \vec{H}^*).$$

Experimentally, the axial impedance is determined by first measuring the phase velocity of the RF wave on the helix circuit, and

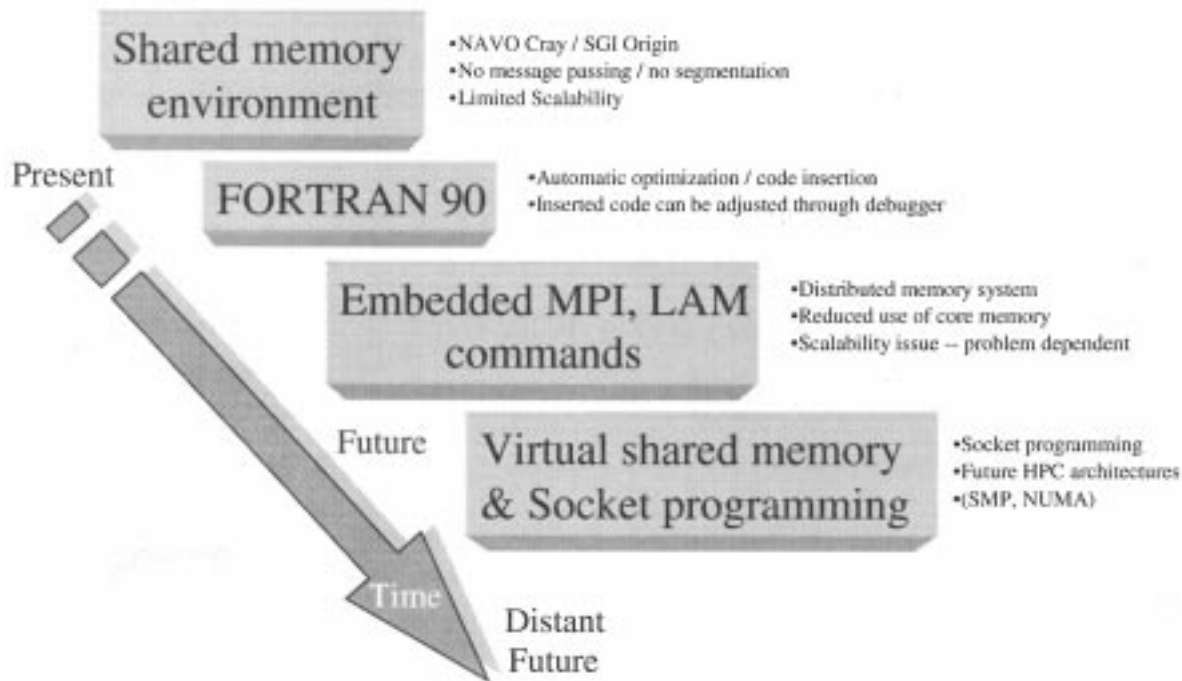


Fig. 18. CTLSS migration to HPC environments.

then inserting a sapphire rod along the axis of the helix and measuring the resulting phase shift and phase velocity with the rod in place. The measured phase shift and the coupling impedance are then related through a perturbation analysis. Fig. 16 depicts a CTLSS setup for the experiment to determine the axial impedance.

Northrop Grumman [44] simulated this experiment with CTLSS to test the approximations in the perturbation method [46] used to compute coupling impedance from perturbed phase velocity measurements. These approximate perturbation expressions were used to evaluate the impedance from both the experimental phase velocity shift as well as CTLSS predictions of the phase velocity shift for the geometry shown in Fig. 16. The goal was to determine whether the perturbation expressions are accurate and independent of rod size even for large values of r_d/r_h , where r_d is the perturbing dielectric rod radius and r_h is the helix radius. Two different rods with $r_d/r_h = 0.24$ and $r_d/r_h = 0.33$ were used for these measurements and simulations. The measurements were carried out using a new single-port measurement method that yielded results that were strongly dependent on rod radius and required further verification with the standard two-port measurement. The CTLSS prediction, however, provided results that are independent of rod size. Fig. 17 shows the comparison between coupling impedance computed directly from the 3-D CTLSS fields and the coupling impedance computed from perturbation theory using the perturbed phase velocity predicted by CTLSS for the two rods mentioned above. It is seen that the perturbation results are independent of rod size and lie close to the direct calculation even for rod sizes up to $r_d/r_h = 0.33$. The discrepancy between the direct calculation and the perturbed results may be because of the approximate nature of the perturbation expressions and given the curves shown in the figure would not

likely yield a result closer to the direct calculation even if a smaller perturbing rod were used.

VII. FUTURE ACTIVITIES—HIGH PERFORMANCE COMPUTING

A. Multiblock Formulation

The current single-block implementation of CTLSS is being extended to multiblock for several reasons:

- 1) Efficient gridding algorithms and commercial gridding tools for nonorthogonal structured grids generally require multiblock configurations.
- 2) Multiblock offers the possibility of avoiding wasted cells in regions where there are no fields.
- 3) Multiblock offers a framework for the eventual parallelization of CTLSS.

The multiblock methodology consists of breaking up the simulation domain into subregions, or blocks, that are connected at interfaces. The solution is carried out in each block volume with the interfaces treated as boundary conditions. As the iterative solution proceeds, the interface data are updated from block to block, e.g., via message passing, so that the solutions in all the blocks converge to a consistent global solution.

How often to update the interface data depends on the latency associated with the transfer of data between blocks. For some systems, with high latency, there may be an advantage in storing multiple layers of overlapped interface cells that are updated less frequently, whereas on low-latency systems, minimal interface overlap with more frequent updates will be more efficient.

B. HPC

The future utilization and acceptance of CTLSS will depend in part on how quickly it will be able to solve large design problems. The growing availability of high-performance computing

(HPC) hardware and software is therefore of major interest in the development of CTLSS. Fig. 18 summarizes the most likely path for applications like CTLSS to migrate onto HPC environments. The present code runs on multiprocessor Cray environments at DoD HPC Major Shared Resource Centers. These centers offer a shared-memory environment with no message passing or segmentation requirements, but have limited scalability to large numbers of processors.

Future implementations will move into multiprocessor environments as improved software, such as Fortran 90, and improved implementations of message-passing interface (MPI) and local-area memory (LAM) protocols become available.

Currently, an inexpensive option for parallel processing is to create a cluster of CPU's linked, for example, by a fast ethernet. SAIC has built an 80-CPU cluster of this type, consisting of 40 dual-CPU machines with shared memory and a fast ethernet back plane. This cluster has demonstrated peak performance of 6–12 Gflops. An activity to port CTLSS to this cluster is in progress. It will begin by porting and running CTLSS on just one of the dual-CPU units. The next step will be to use the multiblock structure being implemented in CTLSS as a means of carrying out domain decomposition so that separate units can work independently on each block during the iterative solution process. Blocks will communicate between processors using MPI commands over the ethernet back plane.

REFERENCES

- [1] L. D. Merkle, R. E. Peterkin, Jr., L. Bowers, L. J. Chandler, S. Colella, A. N. Gibbs, M. H. Frese, P. J. Helles, D. E. Lileikis, J. W. Luginsland, D. T. McGrath, G. E. Sasser, and J. J. Watrous, "Virtual prototyping of RF weapons: A DoD challenge project," in *Proc. 1998 DoD HPCMP Users' Group Conf.*, Rice Univ., Houston, TX, June 1–5, 1998, Session Challenge 1D.
- [2] J. J. Petillo, A. Mankofsky, W. A. Krueger, C. Kostas, A. A. Mondelli, and A. T. Drobot, "Applications of the ARGUS code in accelerator physics," in *Proc. 1993 Computat. Accelerator Phys. Conf., Am. Inst. Phys.*, New York, 1994, pp. 303–312.
- [3] T. Weiland, "On the numerical solution of Maxwell's equations and applications in the field of accelerator physics," in *Particle Accelerators*, vol. 15, pp. 245–292, 1984.
- [4] J. Tückmantel, "An improved version of the eigenvalue processor SAP applied to URMELE," CERN/RF 85-4, 1985.
- [5] R. W. Freund and N. M. Nachtigal, "QMR: A quasiminimal residual method for non-Hermitian linear systems," *Numer. Math.*, vol. 60, pp. 315–339, 1991.
- [6] G. L. G. Sleijpen and H. A. van der Vorst, "A Jacobi–Davidson iteration method for linear eigenvalue problems," *SIAM J. Matrix Anal. Appl.*, vol. 17, pp. 401–425, 1996.
- [7] C. G. J. Jacobi, "Ueber ein leichtes Verfahren, die in der Theorie der Säcularstörungen vorkommenden Gleichungen numerisch auflösen," *Journal für die reine und angewante Mathematik*, pp. 51–94, 1846.
- [8] E. R. Davidson, "The iterative calculation of a few of the lowest eigenvalues and corresponding eigenvectors of large real symmetric matrices," *J. Comput. Phys.*, vol. 17, pp. 87–94, 1975.
- [9] S. J. Cooke and B. Levush, "Eigenmodes solution of 2-D and 3-D electromagnetic cavities containing absorbing materials using the Jacobi–Davidson algorithm," *J. Comp. Phys.*, vol. 157, pp. 350–370, 2000.
- [10] T. M. Antonsen, Jr. and B. Levush, "CHRISTINE: A multifrequency parametric simulation code for traveling wave amplifiers," Naval Res. Lab. Rep. NRL/FR/6840-97-9845, 1997.
- [11] J. Eastwood, W. Arter, N. J. Brealey, and R. W. Hockney, "Body-fitted electromagnetic PIC software for use on parallel computers," *Comput. Phys. Commun.*, vol. 87, pp. 155–178, 1995.
- [12] E. L. Lindman, "'Free Space' boundary conditions for the time dependent wave equation," *J. Comp. Phys.*, vol. 18, pp. 66–78, 1975.
- [13] E. K. Miller, "A selective survey of computational electromagnetics," *IEEE Trans. Antennas Propagat.*, vol. 36, pp. 1281–1305, 1988.
- [14] T. Weiland, "On the numerical solution of Maxwell's equations and applications in the field of accelerator physics," *Part. Accel.*, vol. 15, pp. 245–292, 1984.
- [15] M. Bartsch, M. Dehler, M. Dohlus, F. Ebeling, P. Hahne, R. Klatt, F. Krawczyk, M. Marx, Z. Min, T. Pröpper, D. Schmitt, P. Schütt, B. Steffen, B. Wagner, T. Weiland, S. Wipf, and H. Wolter, "Solution of Maxwell's equations," *Comp. Phys. Commun.*, vol. 72, pp. 22–39, 1992.
- [16] K. S. Yee, "Numerical solution of initial boundary value problems involving Maxwell's equations in isotropic media," *IEEE Trans. Antennas Propagat.*, vol. 14, pp. 302–307, 1966.
- [17] J. P. Berenger, "A perfectly matched layer for the absorption of electromagnetic-waves," *J. Comput. Phys.*, vol. 114, pp. 185–200, 1994.
- [18] W. C. Chew and W. H. Weedon, "A 3D perfectly matched medium from modified Maxwell's equations with stretched coordinates," *Microw. Opt. Technol. Lett.*, vol. 17, pp. 599–604, 1994.
- [19] F. L. Teixeira and W. C. Chew, "General closed-form PML constitutive tensors to match arbitrary bianisotropic and dispersive linear media," *IEEE Microw. Guided Wave Lett.*, vol. 8, pp. 223–225, 1998.
- [20] N. Moiseyev and J. O. Hirschfelder, "Representation of several complex coordinate methods by similarity transformation operators," *J. Chem. Phys.*, vol. 88, pp. 1063–1065, 1988.
- [21] C. W. McCurdy and C. K. Stroud, "Eliminating wavepacket reflection from grid boundaries using complex coordinate contours," *Comput. Phys. Commun.*, vol. 63, pp. 323–330, 1991.
- [22] C. W. McCurdy, C. K. Stroud, and M. K. Wisinski, "Solving the time-dependent Schrödinger equation using complex-coordinate contours," *Phys. Rev. A*, vol. 43, pp. 5980–5990, 1991.
- [23] K. Halbach, "Design of permanent multipole magnets with oriented rare earth cobalt materials," in *Nucl. Instrum. Methods*, vol. 169, 1980, pp. 1–10.
- [24] M. Baird, C.-L. Chang, M. Czarnaski, R. Harper, and D. Holstein, "Investigation of long period focusing for higher average power—Low cost millimeter wave TWT's," Star Microwave Inc. Final Report on Contract F30602-87-C-0216, for RADC (AFSC), Sept. 28, 1989.
- [25] R. H. Jackson, "Off-Axis expansion solution of Laplace's equation: Application to accurate and rapid calculation of coil magnetic fields," *IEEE Trans. Electron Dev.*, vol. 46, pp. 1050–1062, 1999.
- [26] D. Chernin, T. M. Antonsen, Jr., and B. Levush, "Exact treatment of the dispersion and beam interaction impedance of a thin tape helix surrounded by a radially stratified dielectric," *IEEE Trans. Electron Dev.*, vol. 46, pp. 1472–1483, 1999.
- [27] J. R. Pierce, *Traveling Wave Tubes*. Princeton: Van Nostrand, 1950, ch. 7.
- [28] J. H. Wilkinson and C. Reinsch, *Handbook for automatic computation*. Heidelberg: Springer-Verlag, 1971, vol. 2, Linear Algebra.
- [29] O. Axelsson, *Iterative Solution Methods*. Cambridge, U.K.: Cambridge Univ. Press, 1994.
- [30] R. W. Freund and N. M. Nachtigal, "An implementation of the QMR method based on coupled two-term recurrences," *SIAM J. Sci. Comput.*, vol. 15, pp. 313–337, 1994.
- [31] Y. Saad and M. H. Schultz, "GMRES: A generalized minimal residual algorithm for solving nonsymmetric linear systems," *SIAM J. Sci. Stat. Comput.*, vol. 7, 1986.
- [32] R. W. Freund, "A transpose-free quasiminimal residual algorithm for non-Hermitian linear systems," *SIAM J. Sci. Comput.*, vol. 14, pp. 470–482, 1993.
- [33] D. C. Sorensen, "Implicit application of polynomial filters in a k-step Arnoldi method," *SIAM J. Matrix Anal. Applicat.*, vol. 13, pp. 357–385, 1992.
- [34] A. Booten, D. Fokkema, G. Sleijpen, and H. A. van der Vorst, "Jacobi–Davidson methods for generalized MHD-eigenvalue problems," *Z. Angew. Math. Mech.*, vol. 96, pp. 131–134, 1996.
- [35] W. H. Press, S. A. Teukolsky, W. T. Vetterling, and B. P. Flannery, *Numerical Recipes in FORTRAN: The Art of Scientific Computing*, 2nd ed. Cambridge, U.K.: Cambridge Univ. Press, 1992, ch. 11.
- [36] J. Cullum, W. Kerner, and R. Willoughby, "A generalized nonsymmetric Lanczos procedure," *Comput. Phys. Commun.*, vol. 53, pp. 19–48, 1989.
- [37] E. Anderson, Z. Bai, C. Bischof, S. Blackford, J. Demmel, J. Dongarra, J. Du Croz, A. Greenbaum, S. Hammarling, A. McKenney, and D. Sorensen, *LAPACK Users' Guide*, 3rd ed. Philadelphia, PA: Soc. Ind. Appl. Math., 1999.
- [38] S. J. Cooke and B. Levush, "Eigenmode solution of 2-D and 3-D electromagnetic cavities containing absorbing materials using the Jacobi–Davidson algorithm," *J. Comp. Phys.*, vol. 157, pp. 350–370, Jan. 2000.
- [39] J. Descloux, J.-L. Fattbert, and F. Gygi, "Rayleigh quotient iteration, an old recipe for solving modern large-scale eigenvalue problems," *Comput. Phys.*, vol. 12, pp. 22–27, 1998.

- [40] E. R. Davidson, "Super-matrix methods," *Comput. Phys. Commun.*, vol. 53, pp. 49–60, 1989.
- [41] R. W. Freund, M. H. Gutknecht, and N. M. Nactigal, "An implementation of the look-ahead Lanczos algorithm for nonhermitian matrices," *SIAM J. Sci. Comput.*, vol. 14, pp. 137–158, 1993.
- [42] G. L. G. Sleijpen, H. A. van der Vorst, S. Peodts, and J. P. Goedbloed, "Efficient expansion of subspaces in the Jacobi-Davidson method for standard and generalized eigenproblems," *Electron. Trans. Numer. Anal.*, vol. 7, pp. 75–89, 1998.
- [43] R. L. Gluckstern and E. N. Opp, "Calculation of dispersion curves in periodic structures," *IEEE Trans. Magnetics*, vol. 21, pp. 2344–2346, Nov. 1985.
- [44] D. R. Whaley, C. M. Armstrong, and S. J. Cooke, "Initial validation of the CTLSS eigenmode solver in helix geometry," in *Proc. 26th Int. Conf. Plasma Sci.*, Monterey, CA, June 20–24, 1999.
- [45] C. L. Kory and J. A. Dayton, Jr., "Computational investigation of experimental interaction impedance obtained by perturbation for helical traveling-wave tube structures," *IEEE Trans. Electron Dev.*, vol. 45, pp. 2063–2071, Sept. 1998.
- [46] R. P. Lagerstrom, "Interaction impedance measurements by perturbation of traveling waves," Stanford Electron. Lab., Stanford Univ., Stanford, CA, Tech. Rep. 7, 1957.
- [47] J. H. Billen and L. M. Young, "POISSON/SUPERFISH on PC compatibles," in *Proc. 1993 Particle Accelerator Conf.*, vol. 2, 1993, pp. 790–792.

Simon J. Cooke (M'98) was born in Glasgow, U.K., on July 12, 1967. He received the B.Sc. (hons.) degree in physics from the University of Strathclyde in 1988, and the D.Phil. degree from the University of Oxford, in 1992. His doctoral research involved experimental and theoretical analysis of the optical properties of nanoscale organic thin films.

His recent research involves numerical modeling in the area of electron beam and high power microwave physics, at the University of Strathclyde (1992–1995), the University of Maryland (1995–1998), and with Science Applications International Corporation since 1998.

Alfred A. Mondelli was born in New York, NY in 1945. He received the Bachelor's degree in physics from Princeton University, Princeton, NJ, in 1967, and the Ph.D. degree from Cornell University, Ithaca, NY, in 1972.

He was a Postdoctoral Research Associate at the Cornell University Laboratory of Plasma Studies in 1972 and 1973, and a Senior Staff Scientist at Maxwell Laboratories, Inc. from 1973 to 1978. From 1978 to 1980, he worked in the Laser Enrichment Division, Process Physics Group, Exxon Nuclear Company. Since 1980, he has worked at Science Applications International Corporation (SAIC), McLean, VA, where he is currently the Chief Scientist of the Advanced Technology Group. His research interests are centered on the applications of numerical simulation codes for simulation-based design. He was the Manager of the team at SAIC that developed the ARGUS code, a three-dimensional electromagnetic simulation code, and he was active in the MMACE program. His research has included applications of simulation tools in laser isotope separation, ion source development, electromagnetics, ion-projection lithography, vacuum electron devices, and photonics devices. He is currently collaborating with the Naval Research Laboratory on the development of a new generation of simulation tools for vacuum electron devices.

Baruch Levush (M'88–SM'90) received the M.Sc. degree in physics from Latvian University, Riga, and the Ph.D. degree in physics from Tel-Aviv University, Tel-Aviv, Israel.

In 1985, he joined the University of Maryland, College Park, where his research has focussed on the physics of coherent Radiation sources and the design of high power microwave sources, such as gyrotrons, TWT's, BWO's, and free-electron lasers. In 1995, he joined the Naval Research Laboratory (NRL) as head of the Theory and Design Section of the Vacuum Electronics Branch. He is actively involved in developing theoretical models and computational tools for analyzing the operation of existing microwave vacuum devices and in inventing new concepts for high-power, high frequency coherent radiation sources. He is the author and coauthor of more than 100 journal articles.

Dr. Levush is a Member of the American Physical Society.



Thomas M. Antonsen, Jr. (M'87) was born in Hackensack, NJ in 1950. He received the Bachelor's degree in electrical engineering in 1973, and his Master's and Ph.D. degrees in 1976 and 1977, all from Cornell University. He was a National Research Council Post Doctoral Fellow at the Naval Research Laboratory in 1976–1977, and a Research Scientist in the Research Laboratory of Electronics at MIT from 1977 to 1980. In 1980, he moved to the University of Maryland where he joined the faculty of the departments of Electrical Engineering and Physics in 1984. He is currently a Professor of Physics and Electrical Engineering. He has held visiting appointments at the Institute for Theoretical Physics (U.C.S.B.), the Ecole Polytechnique Federale de Lausanne, Switzerland, and the Institute de Physique Theorique, Ecole Polytechnique, Palaiseau, France. He was selected as a Fellow of the Division of Plasma Physics of the American Physical Society in 1986.

Prof. Antonsen's research interests include the theory of magnetically confined plasmas, the theory and design of high power sources of coherent radiation, nonlinear dynamics in fluids, and the theory of the interaction of intense laser pulses and plasmas. He is the author and coauthor of more than 180 journal articles and coauthor of the book *Principles of Free-electron Lasers*. He has served on the editorial board of Physical Review Letters, The Physics of Fluids, and Comments on Plasma Physics.



David P. Chernin received the A.B. (1971) and Ph.D. (1976) degrees in applied mathematics from Harvard University. From 1976 to 1978, he was a Member of the Institute for Advanced Study, in Princeton, NJ, where he worked on problems in magnetic confinement fusion. Since 1984, he has been at Science Applications International Corporation in McLean, VA where he has contributed to multiple research efforts in the theory and simulation of beam-wave interactions in particle accelerators and microwave tubes. Dr. Chernin presently serves as the Manager of the Division of Electromagnetic Science and Engineering at SAIC. He is a Member of the American Physical Society and the Society for Industrial and Applied Mathematics.

Thomas H. McClure received the Bachelor's degree from Georgia Tech. and the Master's degree in mechanical engineering from the University of Dayton. He has more than 15 years experience in analysis, evaluating and testing of spacecraft, aircraft, and launch vehicles. His expertise is in modeling and assessing aerospace vehicle performance characteristics. He is proficient with FAST, GRIDGEN, ICEMCFD, Chemkin, RIPA, GRID3D, IMSL, PVM, F77, F90, FEM's and UNIX codes, and has developed grid generation strategies for NRL electromagnetic analysis and design codes. Mr. McClure is the Technical Lead for the DARPA Next Generation Internet program to explore wireless and high-bandwidth technologies to support Tele-maintenance and Chem-Bio Incident response. He designed and built an 80 CPU, 8 Gigaflop "Beowulf" class super computer. He has reviewed multidisciplinary design, analysis, and system test activities for NASA projects, as well as national mission model requirements for launch vehicle performance capabilities focusing on need for spacecraft design detail. He has influenced ground system requirements definition for testing spacecraft fault tolerant avionics systems, and has assessed operational impact of spacecraft main engine chugging on Cassini mission. He validated Computational Fluid Dynamics codes for application on Ballistic Missile Office and F-117 programs and validated reentry heat transfer test data for BMO High Performance Maneuvering Reentry vehicle. He developed and executed test procedures for spacecraft unique tracking and telemetry data system, and benchmarked hypersonic and combusting flow with GASP, Mercury, and HYLDA and CFD codes.



David R. Whaley (M'96) received the B.S., M.S., and Ph.D. degrees from the Department of Nuclear Engineering at the University of Michigan, Ann Arbor in 1984, 1985, and 1989. His work during this time was focused on the production and characterization of heavy ion charge state distributions in ECR and ICR-heated plasmas in magnetic mirror devices. From 1989–1995, he worked in collaboration with a large international community at the Swiss Federal Institute of Technology in Lausanne, Switzerland developing and testing high-power high-frequency

gyrotron oscillators, developing analytical and computational models of electron beam/RF interactions and performing experiments on RF heating of tokamak plasmas. Dr. Whaley joined Northrop Grumman Corporation in 1995 and is responsible for simulation, design, and test of TWT's for the C-Band and X-Band Microwave Power Module as well as for code development for general vacuum electronics microwave device research. He is also responsible for the technical development of the Northrop Grumman cold cathode electron gun program. Dr. Whaley has authored more than 40 publications on these subjects.

Mark Basten has over ten years experience in the design, development, and testing of high power microwave and millimeter-wave devices. Before joining Northrop Grumman in 1996, Dr. Basten obtained a Ph.D. degree in electrical engineering at the University of Wisconsin-Madison where he specialized in the development of novel slow-wave microwave devices utilizing high-perveance sheet electron beams. Dr. Basten also has extensive experience in the development of high power millimeter-wave gyrotron tubes, including the development of a tunable 130–145 GHz gyro-BWO, the design of a 94 GHz gyro-TWT, and has conducted experimental studies of parasitic modes in MW-level gyrotrons and beam diagnostics. At Northrop Grumman, Dr. Basten has been responsible for the development of a number of moderate-power, multi-octave TWT's as well as introducing improved simulation tools for helix TWT circuit and collector design. Dr. Basten also leads internal R&D efforts to investigate advanced solid state emitters and novel submillimeter-wave devices.